Pontifícia Universidade Católica
do Rio de Janeiro

Nicole Lopes Monteiro de Barros Junqueira

Assessment of reduced order models applied to steady-state bi-dimensional laminar methane air diffusion flame

Dissertação de Mestrado

Dissertation presented to the Programa de Pós–graduação em Engenharia Mecânica, do Departamento de Engenharia Mecânica da PUC-Rio in partial fulfillment of the requirements for the degree of Mestre em Engenharia Mecânica.

Advisor : Prof. Igor Braga de Paula
Co-advisor: Dr. Luís Fernando Figueira da Silva
Co-advisor: Dr. Louise da Costa Ramos

Rio de Janeiro
February 2022

Pontifícia Universidade Católica
do Rio de Janeiro

Nicole Lopes Monteiro de Barros Junqueira

Assessment of reduced order models applied to steady-state bi-dimensional laminar methane air diffusion flame

Dissertation presented to the Programa de Pós–graduação em Engenharia Mecânica da PUC-Rio in partial fulfillment of the requirements for the degree of Mestre em Engenharia Mecânica. Approved by the Examination Committee:

Prof. Igor Braga de Paula
Advisor
Departamento de Engenharia Mecânica – PUC-Rio

Dr. Luís Fernando Figueira da Silva
Co-advisor
Departamento de Engenharia Mecânica – PUC-Rio

Dr. Louise da Costa Ramos
Ansys - France

Dr. Valéry Morgenthaler
Ansys - France

Prof. Florian Alain Yannick Pradelle
Departamento de Engenharia Mecânica – PUC-Rio

Rio de Janeiro, February the 17th, 2022

Nicole Lopes Monteiro de Barros Junqueira

Graduated in Mechanical Engineering at Pontifícia Universidade Católica do Rio de Janeiro - PUC-Rio (Rio de Janeiro, Brazil), 2020.

Bibliographic data

Junqueira, Nicole Lopes Monteiro de Barros

Assessment of reduced order models applied to steady-state bi-dimensional laminar methane air diffusion flame / Nicole Lopes Monteiro de Barros Junqueira; advisor: Igor Braga de Paula; co-advisores: Luís Fernando Figueira da Silva, Louise da Costa Ramos. – 2022.

76 f: il. color. ; 30 cm

Dissertação (mestrado) - Pontifícia Universidade Católica do Rio de Janeiro, Departamento de Engenharia Mecânica, 2022.

Inclui bibliografia

1. Engenharia Mecânica – Teses. 2. Aprendizado de máquina. 3. Dinâmica dos fluidos computacional. 4. Chamas não pré-misturadas. 5. Combustão de metano/ar. I. Paula, Igor Braga de. II. Silva, Luís Fernando Figueira da. III. Ramos, Louise da Costa. IV. Pontifícia Universidade Católica do Rio de Janeiro. Departamento de Engenharia Mecânica. V. Título.

CDD: 621

Acknowledgments

I would like to thank my parents, Dinorá Cristina Lopes and Claudio Junqueira, and my sister, Livia Junqueira, for their support, encouragement, friendship and unconditional love. There are no words to thank them enough, without them I would not achieve even half of my dreams. I am also grateful to my grandparents, Marly and Henrique for everything, thank you for the encouragement in all steps of my life.

I would like to thank my co-advisors, Luís Fernando Figueira da Silva and Louise da Costa Ramos, for their friendship, encouragement, knowledge, experience, and patience. And to professor Igor Braga de Paula, for having joined this project as my supervisor, for all his suggestions and insights.

I would like to thank my friends, Karina Riccio, Lays Santos, Carolina Mello, Natália Gautreaux, Priscila Nery, Isabelle Rocha, Matheus Hoffmann, Matheus Suknaic, Flávia Sanfins. Thank you for all the happy moments, for the laughs and companionship all the time. Thanks Lenon Soares, who five years ago started as my English teacher and today I consider a friend for life, thanks for the chats, patience, and for the countless rehearsals of any conference presentation. And to my friends and colleagues in the lab, Caroline and Maria Clara, for encouraging and helping me throughout the course and for the relaxing moments.

Finally, I would like to thank everyone who collaborated in any way in the realization of this work.

I am also grateful to Dr. Valéry Morgenthaler (Ansys/France) for his collaboration and partnership in this work. This study was financed in part by the Coordenação de Aperfeiçoamento de Pessoal de Nível Superior - Brasil (CAPES) - Finance Code 001.

Abstract

Junqueira, Nicole Lopes Monteiro de Barros; Paula, Igor Braga de (Advisor); Silva, Luís Fernando Figueira da (Co-Advisor); Ramos, Louise da Costa (Co-Advisor). **Assessment of reduced order models applied to steady-state bi-dimensional laminar methane air diffusion flame**. Rio de Janeiro, 2022. 76p. Dissertação de Mestrado – Departamento de Engenharia Mecânica, Pontifícia Universidade Católica do Rio de Janeiro.

Computational fluid dynamics (CFD) is often applied to the study of combustion, enabling to optimize the process and control the emission of pollutants. However, reproducing the behavior observed in engineering systems has a high computational burden. To overcome this cost, machine learning techniques, such as reduced order models (ROM), have been applied to several engineering applications aiming to create models for complex systems with reduced computational cost. Here, the ROM is created using CFD laminar non premixed flame simulation data, decomposing it, and then applying a machine learning algorithm, creating a static ROM. This work analyzes the effect of five different data pre-processing approaches on the ROM, these being: (1) the properties treated as an uncoupled system or as a coupled system, (2) without normalization, (3) with temperature and velocity normalized, (4) all properties normalized, and (5) the logarithm of the chemical species. For all ROM constructed are analyzed the energy of the reduction process and the reconstruction of the flame properties fields. Regarding the reduction energy analysis, the coupled ROM, except the ROM (4), and the logarithm ROM converges faster, similarly to the uncoupled temperature ROM, whereas the uncoupled minor chemical species ROM exhibits a slower convergence, as does the coupled ROM with all properties normalized. So, the learning is achieved with a smaller number of modes for the ROM (2), (3) and (5). As for the reconstruction of the property fields, it is noted that there are regions of negative mass fraction, which suggest that the ROM methodology does not preserve the monocity or the boundedness of the properties. The logarithm approach shows that these problems are overcome and reproduce the original data.

Keywords

Machine learning; Computational fluid dynamics; non-premixed flames; methane/air combustion.

Resumo

Junqueira, Nicole Lopes Monteiro de Barros; Paula, Igor Braga de; Silva, Luís Fernando Figueira da; Ramos, Louise da Costa. **Avaliação de modelos de ordem reduzida aplicados à simulação bidimensional em regime estacionário de chamas laminares de difusão de metano e ar**. Rio de Janeiro, 2022. 76p. Dissertação de Mestrado – Departamento de Engenharia Mecânica, Pontifícia Universidade Católica do Rio de Janeiro.

Dinâmica dos Fluidos Computacional (CFD) é frequentemente aplicada ao estudo da combustão, permitindo otimizar o processo e controlar a emissão de poluentes. Entretanto, reproduzir o comportamento observado nos sistemas de engenharia tem uma elevada carga computacional. Para superar este custo, técnicas de aprendizagem de máquinas, tais como modelos de ordem reduzida (ROM), têm sido aplicadas a várias aplicações de engenharia com o objetivo de criar modelos para sistemas complexos com custo computacional reduzido. Aqui, o ROM é criado usando dados de simulação de chama laminar não pré-misturada de CFD, decompondo-os, e depois aplicando um algoritmo de aprendizagem de máquinas, criando um ROM estático. Este trabalho analisa o efeito de cinco abordagens diferentes de pré-processamento de dados sobre o ROM, sendo estas: (1) as propriedades tratadas como um sistema desacoplado ou como um sistema acoplado, (2) sem normalização, (3) com temperatura e velocidade normalizadas, (4) todas as propriedades normalizadas, e (5) o logaritmo da espécie química. Para todos os ROM construídos são analisados a energia do processo de redução e a reconstrução dos campos das propriedades da chama. Em relação a análise da energia da redução, o ROM acoplado, exceto o ROM (4), e o ROM do logaritmo convergem rapidamente, semelhante ao ROM da temperatura desacoplado, enquanto o ROM da espécie química minoritária desacoplado exibe uma lenta convergência, tal como o ROM acoplado com todas as propriedades normalizadas. Assim, a aprendizagem é atingida com um número menor de modos para a ROM (2), (3) e (5). Quanto à reconstrução dos campos de propriedades, nota-se que existem regiões de fração mássica negativa, o que sugere que a metodologia do ROM não preserva a monotonicidade ou a delimitação das propriedades. A abordagem do logaritmo mostra que estes problemas são superados e reproduzem os dados originais.

Palavras-chave

Aprendizado de máquina; Dinâmica dos fluidos computacional; Chamas não pré-misturadas; Combustão de metano/ar.

Table of contents

List of figures

List of tables

List of Symbols

Latin symbols

A – frequency factor or preexponential factor

$\mathbf{A}$ – data matrix

A_{cell} – cell area

$\widehat{A}_m$ – aggregation of the m surrogates models

D – Diameter

$D_{i,j}$ – binary diffusion coefficient for species i and j

$D_{T,i}$ – thermal diffusion coefficient for species i

E_a – activation energy

e – specific internal energy

e_{i1} – error indicator

Fr – Froude number

$\mathbf{f}_i$ – body force

$\vec{g}$ – gravity acceleration vector

h_i – specific entalpy of species i

k – bulk viscosity coefficient

k_f – specific reaction rate constant

L_e – hydrodynamic entrance length

L_f – computed flame length

n – max level of refinement

$\mathbf{P}$ – stress tensor

p – pressure

$\mathbf{q}$ – heat flux vector

$\mathbf{q}_r$ – radiant heat flux vector

Re – Reynolds number

r – gradient volume weight

r_{Y_i} – residual mass fraction

R_i – reaction rate

R_i^* – approximated reaction rate

R° – universal gas constant

S – font term

$\hat{s}$ – surrogates models

T – temperature

T_{ad} – adiabatic flame temperature

T_o – fresh gas temperature

T^* – normalized temperature

U – unitary matrix/left singular vectors

$\mathbf{U}$ – unit tensor

u – velocity component

u_o – air inlet velocity

u^* – normalized velocity

V^T – transpose of the right singular vectors

$\mathbf{V}_i$ – diffusion velocity of species i

$\vec{v}$ – velocity vector

$\mathbf{v}$ – velocity

$v_{z|a,in}$ – prescribed air inlet velocity

$v_{z|f,in}$ – prescribed fuel inlet velocity

v_x – axial velocity component

v_y – radial velocity component

W_i – molar mass of species i

$\overline{W}$ – average molar mass

X_i – mole fraction of species i

Y_i – mass fraction of species i

$Y_{i,max}$ – maximum value of Y_i

Y^* – species mass fraction normalized

$\hat{Y}_i$ – mass fraction after truncation parameter ϵ_c

$\overline{Y}_i$ – logarithm of $\hat{Y}_i$

Greek symbols

Γ – diffusion term

ϵ_c – truncation parameter

λ – thermal conductivity

μ – viscosity

ρ – density

Σ – singular values matrix

τ – approximate time-step

ϕ – convective term

ω_i – mass reaction rate

ω_l – GARS weight
$\hat{\omega}_i$ – molar reaction rate

1
Introduction

In this chapter, the motivation and context of this study are introduced. Thus, the principles of laminar non-premixed flames, the Gülder burner, and applications of computational fluid dynamics with an emphasis on combustion are briefly described. Particular emphasis is given on the various applications of machine learning techniques, especially in engineering and associated problems, such as modelling combustion systems.

1.1
Laminar non-premixed flames

The combustion process is present in different applications, from industrial processes, the major transportation vehicles, until the most simple application, such as the kitchen stove. Therefore, one of the issues of concern in this area is the emission of pollutants from the combustion process of fossil fuels which is harmful to human health and to the environment [1, 2, 3].

Combustion is a complex process involving heat and mass transfer, chemical kinetics, thermodynamics, and fluid dynamics [4]. This process involves an exothermic chemical reaction between a fuel and an oxidant that releases energy in the form of heat. Subsequently, the released energy can be transformed into electrical or mechanical energy.

Classically, flames are classified into two groups; the premixed and the non-premixed flames. The main difference regards the mixture between the fuel and oxidant, at the molecular level, which happens or not prior to the chemical reaction [4]. On the one hand, in premixed flames, the reactants are homogeneously mixed before the reaction takes place. On the other hand, in the non-premixed flames, the mixing is not fast enough, so the fuel and oxidant are initially separated. A simple example of non-premixed combustion is a candle flame [5].

In non-premixed flames, which are of interest in this work, the transport of fuel and oxidant happens due to diffusion and the bulk convective motion of the reaction region. As a consequence, the reaction between the substances occurs rapidly, and the combustion products together with the heat released are transported away from the reactive zone. Since the combustion is usually considered a fast reaction, the non-premixed flame is often controlled by the stoichiometric rates of transport of fuel and oxidant to the reaction sheet [4].

Moreover, another classification concerns the nature of the flow, i.e., whether it is laminar or turbulent. In laminar flows, there are distinct streamlines for convective motion, in other words there is no mixing at the macroscopic scale (only diffusion) [6]. Whereas in turbulent flow the nature of turbulence causes the flow to fluctuate in the three dimensions of the space in time at any point in space [6]. Indeed, this turbulence phenomenon eventually facilitates the process of coarse mixing, which has a considerable influence on non-premixed flames, as mixing the reactants is essential. In this study, laminar non premixed flames will be the subject of interest only.

The combustion process is a multi-scale phenomenon, which means that different processes occur at time scales, spanning several orders of magnitude. Due to the diffusion present in flames, these time scales manifest as length scales also [4]. However, most computational methods developed to solve turbulence problems, originally created for non-reacting flows, treats the turbulence phenomenon as a single-scale problem [7, 8]. When applied to the description of turbulent flames, the multi-scale nature of combustion is often ignored [9]. In this sense, the numerical description of the multi-scale nature of laminar non premixed flames requires the use of more complex methodologies than for turbulent combustion.

Indeed, one of the concerns regarding the hydrocarbon/air combustion process is the emission of effluents, such as NO_x and soot. In the case of soot, which is a solid particulate material from the combustion of gaseous fuels, its production can be affected by the flow regimes, pressure, for instance. [4]. It is well known that non-premixed flames produce more soot when compared to fuel-lean premixed flames. This can be explained, in the case of premixed flames, by the existence of oxidizing elements at the region where soot formation proceeds, i.e., where the breakdown of fuel molecules occurs [1, 4].

Gülder burner

Willing to study of soot formation, the well-known Gülder burner has been often used for experiments, since it has a simple geometry and is widely used for stable, axisymmetric, non-premixed laminar flames [10, 11, 12]. Moreover, the non-premixed flame stabilized on this burner, when compared with others, produces a higher volumetric fraction of soot. For this reason, industrial burners are often represented by the Gülder burner for the purpose of studying soot formation and oxidation processes [13]. Accordingly, this burner geometry is of interest here, even if soot formation is not.

The burner presents an axial symmetry flow and two inlets [11], as shown in Fig. 1.1a. The fuel enters through the central tube, which diameter is 11 mm, and the air enters through an annular region with a radius of 50 mm, being responsible for the flame stabilization. Figure 1.1b shows an ethylene/air laminar diffusion flame stabilized on a Gülder burner [11].


(a) (b)

Figure 1.1: (a) Representation of the Gülder burner and (b) Ethylene/air flame stabilized on the Gülder burner [11].

One of the first purposes of this burner was to compare the effects of nitrogen dilution and flame temperature on soot formation in ethylene diffusion flames [10]. More recently, studies on the Gülder burner have been done focusing on the soot formation characteristics in non-premixed laminar flames of a volumetric mixture of n-heptane/butanol isomer and air, and soot characterization when ammonia is diluted to n-heptane fuel [14, 15]. The focus of the present work is not on comparing computational and experimental results, despite the existing soot formation data available, rather a model of a non sooting flame is of interest only.

Numerical applications

It is well know that, as the system under study becomes more complex, the cost of experimental research is increased. This is related to the time and expenses of the experiments, such as the cost of the experimental set-up and the raw materials, or the time to calibrate all the measuring equipment. Therefore, numerical techniques are often used to analyze different properties using computer simulations. For instance, the computational fluid dynamics (CFD), which is a tool widely used to analyze complex flow problems that are of interest to industry, such as combustion processes and aerodynamic problems [16]. Recently, such numerical methodology was used, for instance to investigate the dispersion and generation of turbulence, using a 3D geometry, of flammable dust mixtures which that can cause accidents in the pharmaceutical and chemical manufacturing industries [17]. Also, the numerical investigation of immiscible droplets spread on a thin liquid substrates, with the fluid volume technique, coupled with the piecewise linear interface calculations method, was applied to obtain a time evolution of the droplet dynamics [18]. For different unmanned aerial multi-rotor vehicles, CFD simulation with high-order accurate schemes were performed to understand the complex flow associated to such engines, thus facilitating the design for a more efficient, safer and quieter aerial vehicle [19]. Those are a few examples only of the pervasive use of CFD to solve a plethora of science and engineering problems.

Concerning the use of CFD in combustion, it has enabled the analysis of different flow properties, such as the species mass fraction and temperature distribution. However, a faithful description of flames, needs to describe detailed chemical mechanism of the combustion process, and consequently the chemical kinetics related to the fuel oxidation. Furthermore, the detailed mechanism, and its different time and length scales, introduce a significant computational burden related to the simulation time and memory demanded [20]. Therefore, performing a CFD parametric study of combustion processes is often not feasible. Therefore, the application of artificial intelligence, machine learning, and data driven techniques to engineering problems is becoming important to overcome this computational shortcoming [21, 22, 23].

1.2
Machine learning

Machine learning (ML) is an evolving branch of computational algorithms. In particular, it include models that improve from different available data, and which are based on fundamental mathematics, linear algebra, optimization, and regression [24]. In other words, ML are algorithms which performance improves as it is exposed to more data. Ideally, ML generalizes the given data, learning its patterns and correlating them with the outcomes that are intended to be predicted in the field. Once the model is validated, it can be applied, to new database values [25]. Examples of machine learning include identifying objects in images, selecting relevant search results, and machine translation [26].

These learning algorithms can be classified according to their structure, which can be supervised or unsupervised, depending on the information available to the model [25]. Supervised learning is the most common form of ML, where the goal is to make predictions of a target by having expert knowledge learning, providing corrective information to the algorithm [26]. In unsupervised approach, the learning occurs without training data being labeled, where the goal is to find a structure in the data [25, 24].

Regarding the data used in the learning process, machine learning approaches can be divided into two groups, online and offline. Online models learn the characteristics of the system while the data is being collected, e.g., artificial neural networks applied to image recognition [26]. Concerning fluid dynamics applications, the estimation of the eddy viscosity has been developed using online identification, which enabled an adaption of a reduced order model to changes of the flow configuration [27]. On the contrary, offline models learn the behavior based on previously collected data. For instance, the ROM of the Navier-Stokes equations of a flow passing a cylinder has used an offline data collection [28].

The machine learning application field embraces different fields of knowledge, such as engineering, biomedical, and finance [29, 30, 31]. For example, the ML has already been applied to the analysis of genome sequencing data sets or applications in agricultural supply chains in different phases [32, 33]. However, such algorithms are not yet widely accepted in the operation of engineering systems because they are often considered to be black-box models, i.e., the algorithms learn without prior knowledge about the underlying physics of the problem or its restrictions [26, 34]. To overcome such limitation, it has been proposed to combine ML with first principles models of a engineering systems [34, 35]. An example is the physics-informed machine learning used to predict the critical heat flux with superior performance over standalone approaches [36].

Concerning the combustion process, machine learning techniques applications have been used for over a decade, as highlighted in reviews [21, 38]. A reduced order model based on CFD simulations results for oxy-coal combustion enabled the estimation of the average outlet temperature of the burned gases for a given fuel and oxidant mass flow rates, and also to determine the inlet mass flow rate required to obtain the desired temperature [39]. However, the application of a non-intrusive reduced order model for an unstable flow using an approach which combines the POD with a feed-forward neural network [40]. Recently, a non-intrusive methodology, using the proper orthogonal decomposition and an interpolation method, has been applied to construct a digital twin using CFD simulations and real-time measurements of an industrial system [41].

Reduced order model is a ML technique, which starts with the application of a reduction method to the data. For instance, singular value decomposition (SVD) or proper order decomposition (POD) are usually applied as reduction methods, and then an interpolation/integration method is applied to learn the behavior of the system. As an example, the application of the POD approach for a ROM of the Navier-Stokes equation was used with different methods of integration/interpolation, and then, the results were compared [28]. Another recent application of the reduction method SVD was used coupled with the interpolation method genetic aggregation response surface (GARS) to predict the behavior of a laminar premixed inverted conical flame [37].

The particular application of reduced order model techniques to combustion covered different problems, such as the description of flame properties of a laminar premixed flame, where steady CFD reactive simulations were used to create the ROM, and also, the analysis of the infrared radiation emitted by a reacting, supersonic, turbulent jet that used numerical simulation to construct the ROM dataset [37, 42]. Furthermore, an approach that blends data-driven learning with the theoretical foundations was proposed for a single injector combustor of a rocket engine to predict the properties profiles, such as pressure and temperature [23]. For a similar problem, a physics-based data-driven method was proposed to learn the physics of a single-injector combustor ROM using high-fidelity simulations [43].

Even if turbulent flames typifies most practical combustion industrial processes, the multi-scale physics of laminar flames enables the study of combustion from the perspective of the computational cost of high-fidelity CFD simulations. The associated multiple time and length scales present in such flames increase the complexity of the models and of the learning process. Furthermore, the application of reduced order model methodology is not as explored for laminar non-premixed flames, as it is for turbulent flames [37, 21].

1.3
Objectives

This work has been developed in the context of a partnership between Ansys/France and PUC-Rio which is devoted to the study of reduced order models applied to combustion problems. The general goal of the present study is the development of reduced order models for multi-scale combustion processes. More precisely, the reconstruction of flame properties and the issue concerning the monotonicity of the reduced model reconstructed properties are studied here.

The main objective of this work is to develop reduced order models of methane/air laminar non-premixed flame stabilized on a Gülder burner, using CFD results to construct ROM. The corresponding specific objectives are:

- To analyze the influence of pre-processing the learning data, which are the CFD modelled combustion properties, on the ROM results, i.e.,:

    - The impact of creating a ROM for each uncoupled flame property or treating the properties as a coupled system;
    - The effect of normalizing the data set, including the species data since some minority species mass fraction are of the order of magnitude of 10^{-6};
    - The influence of applying a logarithm transformation of species mass fraction to construct the ROM;
- To develop an analysis of the reconstructed modes energy content of each methodology applied to the learning data;
- To compare the CFD and ROM results.

1.4
Manuscript organization

This work is organized in four chapters:

1. Introduction: motivation and objectives;

2. Numerical methodology: A brief description of the mathematical formulation of the conservation equations for a combustion problem. The boundary conditions applied to the burner, the mesh and computation domain used. The methodology for reduced order models and the studied learning data pre-processing.

3. Results and Discussion: A brief discussion of the flame configuration and the computational fluid dynamics result for a validation case. The discussion regarding the properties profiles reconstruction and the analysis of the reconstructed modes energy content for the different reduced order models created.

4. Conclusions and Perspectives: The conclusions and perspectives for future works are discussed.

2
Numerical methodology

In this chapter, the proposed numerical methodology is presented. First, the procedure used to model a non premixed flame is described in terms of the main equations, the domain of interest and the computational domain meshing and solution procedures. Then, the steps to construct a reduced order model are described: the collection of data; application of an algorithm of data reduction; separate the data according its importance; and interpolate the reduced data.

2.1
Mathematical formulation

The equations for solving a fluid flow with heat and mass transfer may be summarized by the solution of the general transport equation [7].

$$\frac{\partial(\rho\phi)}{\partial t} + \nabla \cdot (\rho\vec{v}\phi) = \nabla \cdot (\Gamma\nabla\phi) + S. \tag{2-1}$$

The first term represents the transient effect, the second and third terms represent the convection and diffusion effects, respectively, and the source term is the last one. The properties ϕ, Γ and S change according to the conservation equation considered, and ρ represents the density. The present flow modeling involves the solution of the conservation equations of total mass, energy, momentum and individual species, which are written as [4]:

$$\frac{\partial\rho}{\partial t} + \nabla \cdot (\rho\mathbf{v}) = 0, \tag{2-2}$$

$$\rho\frac{D\mathbf{v}}{Dt} = -\nabla \cdot\ \mathbf{P} + \rho\sum_{i=1}^{N}(Y_i\mathbf{f}_i), \tag{2-3}$$

$$\rho\frac{De}{Dt} = -\nabla \cdot\ \mathbf{q} - \mathbf{P} : (\nabla \cdot\ \mathbf{v}) + \rho\sum_{i=1}^{N} Y_i\mathbf{f}_i \cdot\ \mathbf{V}_i, \tag{2-4}$$

$$\rho\frac{DY_i}{Dt} = \omega_i - \nabla \cdot (\rho Y_i\mathbf{V}_i), \quad i = 1, ..., N. \tag{2-5}$$

In the total mass conservation, Eq. (2-2), there are transient and convective terms, i.e., the mass variation with time and the net mass flow. However, there is no diffusion and neither a source term, so $\phi = 1$, and the terms Γ and S are null. At the linear momentum equation, Eq. (2-3), ϕ is the velocity ($\mathbf{v}$), Γ is the viscosity μ and S contains a part concerning the body force ($\mathbf{f}_i$), the pressure gradient and one viscous part. The influence of viscosity μ and the pressure appear by expanding the stress tensor ($\mathbf{P}$) as [4]:

$$\mathbf{P} = \left[p + \left(\frac{2}{3}\mu - k\right)(\nabla \cdot \mathbf{v})\right]\mathbf{U} - \mu\left[(\nabla \mathbf{v}) + (\nabla \mathbf{v})^T\right], \tag{2-6}$$

where p is the hydrostatic pressure, k is the bulk viscosity coefficient, $\mathbf{U}$ is the unit tensor, and the superscript T is the matrix transpose. Thus, relating the viscous stress with the strain rate for Newtonian fluids. Note that the coefficient k, the bulk viscosity, is often neglected, but not necessarily in combustion cases, since the density variation is large [4, 44].

The energy conservation equation, Eq. (2-4), includes the chemical model, sensible and flow kinetic energies. The energy sources that can change the internal energy are due to the energy flux incident at the boundary, the work done on the system by the surface forces and by the body forces [4]. The heat flux vector ($\mathbf{q}$) is influenced by the heat transfers through: conduction in the presence of temperature gradient; mass diffusion due to different heat contents of species; the second-order diffusion, the Dufour effect; and the radiation heat transfer vector, that is important for flames with heavy soot loading [4, 45]. This term may be written as:

$$\mathbf{q} = -\lambda \nabla T + \rho \sum_{i=1}^{N} h_i Y_i \mathbf{V}_i + R^o T \sum_{i=1}^{N}\sum_{j=1}^{N}\left(\frac{X_j D_{T,i}}{W_i D_{i,j}}\right)(\mathbf{V}_i - \mathbf{V}_j) + \mathbf{q}_r, \tag{2-7}$$

where λ is the thermal condutivity, h_i is the specific entalpy of species i, R^o is the universal gas constant, W_i is the molecular weight of species, and $D_{i,j}$ is the binary diffusion coefficient for species i and j. The radiant heat flux ($\mathbf{q}_r$) accounts for the radiation effect in all directions, it depends on the temperature as on the nature of the participating medium. This radiation term is important for flames with heavy soot loading, i.e., for problems where there is large formation of soot, such as furnace or wildland fires [4, 1]. The species diffusion velocity may be computed by solving:

$$\begin{gathered}\nabla X_i = \textstyle\sum_{j=1}^{N}\left(\frac{X_i X_j}{D_{i,j}}\right)(\mathbf{V}_j - \mathbf{V}_i) + (Y_i - X_i)\left(\frac{\nabla p}{p}\right) + \left(\frac{\rho}{p}\right)\sum_{j=1}^{N} Y_i Y_j (\mathbf{f}_i - \mathbf{f}_j) \\ + \textstyle\sum_{j=1}^{N}\left[\left(\frac{X_i X_j}{\rho D_{i,j}}\right)\left(\frac{D_{T,j}}{Y_j} - \frac{D_{T,i}}{Y_i}\right)\right]\left(\frac{\nabla T}{T}\right),\end{gathered} \tag{2-8}$$

where $\mathbf{V}_i$ is the diffusion velocity.

Equation (2-8) is derived from the multi-component transport theory, and shows that mass diffusion in the presence of four terms is respectively influenced by: the concentration gradient; a pressure gradient (barodiffusion); body forces gradient, such as an electromagnetic field; and a temperature gradient (Soret effect or thermophoresis)[4]. The Soret diffusion coefficient

$(D_{T,i})$ represents the influence on the molecular transport of the temperature gradient.

Regarding the species transport equations, it considers the Soret thermal diffusion effect, which influences the diffusion velocity $(\mathbf{V}_i)$ [46, 47]. Such effect causes heavy molecules to diffuse less rapidly, and light molecules to diffuse more rapidly, towards heated surfaces and includes the effect of enthalpy transport due to species diffusion in the energy equation [48]. Note that classical mixing law formulations are used to determine the transport properties as a function of temperature, composition and pressure [4].

In Eq.(2-5), ω_i is the mass reaction rate, which is related to the molar reaction rate $\hat{\omega}_i$ through $\omega_i = W_i \cdot \hat{\omega}_i$, where W_i is the molar mass. The molar reaction rate is expressed by the Arrhenius' law, which describes the chemical kinetics rate, enabling to determine the variation in the specific reaction rate constant with temperature. Assuming a single, forward chemical reaction represented by:

$$\sum_{i=1}^{N} a_i M_i \overset{k_f}{\rightarrow} \mathit{products}, \tag{2-9}$$

where M_i represents the chemical species i and a_i is the corresponding molar concentration coefficient, k_f is the specific reaction rate constant, and the subscript f denotes the direction of this reaction, in this case the forward one. It is important to emphasize the existence of reversible reactions, also present in the combustion process, in which associated to every forward reaction there is a corresponding backward reaction [4, 44].

In order to relate, the rates of change in the molar concentration of the chemical species in a reaction, such as Eq. (2-9), is used the reaction rate (ω), which is proportional to the product of the concentrations of the reactants [4]:

$$\omega = k_f(T) \prod_{i=1}^{N} [M_i]^{a_i}. \tag{2-10}$$

The dependence of the reaction rate on temperature requires the reaction rate specification, which is given by the Arrhenius law [4]:

$$k_f(T) = A e^{(-E_a/R^o T)}, \tag{2-11}$$

where E_a is the reaction activation energy, A is a frequency factor (preexponential) and R° is the universal gas constant.

In order to simplify the equations to be solved, hypotheses are applied to the problem considered, i.e., the steady state combustion process and incompressible fluid. This allows to neglect the time derivative terms in Eqs. (2-2) - (2-5). Another important hypothesis is that all gases present in the combustion process are perfect gases. This enables relating the pressure (p)

to the temperature (T), density, universal gas constant and the average molar mass ($\overline{W}$):

$$p = \rho R^{\circ} T / \overline{W}, \tag{2-12}$$

where $\overline{W} = \sum X_i W_i$. For instance, in the case of an open system that does not have any pressure forcing, the influence of the pressure might be ignored, causing the product ρ and T to be constant, thus, ρT is strongly coupled. Tab. 2.1 summarizes the hypotheses used to solve the equations and the equations where it interferes.

Table 2.1: The hypotheses used and the equations it directly interferes with.

Hypotheses		Equations
steady state	$\partial(\ )/\partial t = 0$	2-2; 2-3; 2-4; 2-5
incompressible flow	$\rho =$constant	2-2; 2-3; 2-4; 2-5
perfect gas	-	2-12
absence of gravity	$\vec{g} = 0$	2-3 ; 2-4
absence of radiation	$\mathbf{q_r} = 0$	2-4

2.1.1
Chemical reaction mechanism

It is possible to determine the final state of the combustion process based on the initial state and using chemical and thermodynamic equilibrium such as minimization of free Gibbs energy and equilibrium constant calculations. However, in such an approach the reactions paths that lead the initial mixture to the obtained products, or the time it takes, are not available. This is why the detailed knowledge of the chemical reaction paths is required when combustion process details are of interest, which is the case here. Figure 2.1 illustrates some reaction pathways for a typical detailed kinetic mechanism of methane oxidation. The use of detailed chemistry is necessary when modeling controlled kinetic phenomena, such as the slow formation of products and pollutant species, and the ignition and extinction of flames.

In this work, the chemical reactions in the methane/air flames and its time scales are accounted for using a skeletal kinetic mechanism, called DRM19. Such reduced kinetics, based on the detailed GRI-Mech 1.2, contains 19 species plus N_2 and Ar and 83 chemical reactions [49]. Since Eq. (2-5) is the conservation of individual species, for this mechanism, it is solved for all 21 species. Thus, the combustion calculations involve a significant computational burden, when compared to the solution of pure fluid problems.

By comparing the methane oxidation pathways in Fig. 2.1 against the reactions in the DRM19 mechanism, it is seen that all chemical species are

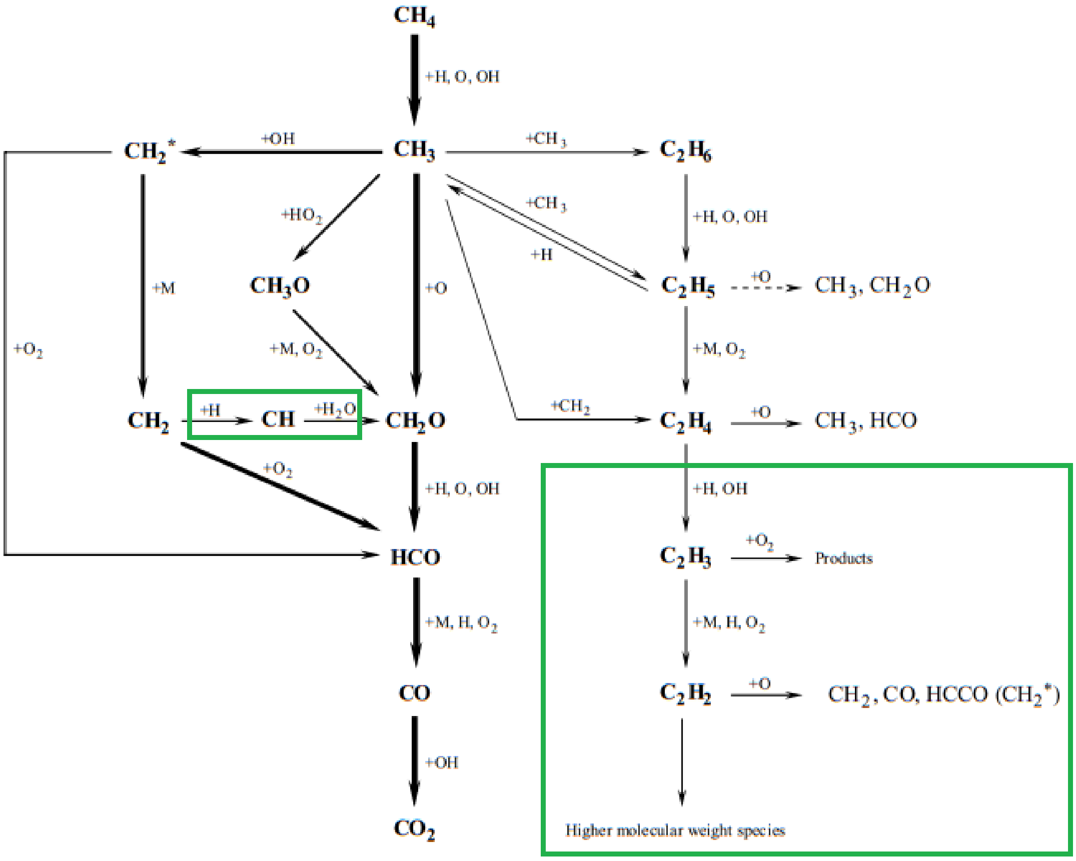

Figure 2.1: Reaction paths in methane flames, where the thickness of the arrows indicates the importance of individual pathways [4]. The green rectangles represent the paths not found in the DRM19 mechanism.

present in the mechanism except: CH; C_2H_3 and C_2H_2. The absence of C_2H_2 makes it unsuitable to predict the formation of high molecular weight species, such as soot, since acetylene is the precursor of the formation of benzene and higher molecular weight aromatics in hydrocarbon combustion. The CH_2^* is the highly active singlet methylene radical, which is de-energized from collisions with molecules, in the case of Fig. 2.1; M or O_2, becoming the CH_2, which is more stable, and the HCO, respectively. In DRM19, CH_2^* also forms CH_3; C_2H_4; CO and CH_2O. Another difference is the oxidation of carbon monoxide, such that the DRM19 mechanism has three additional reactions beyond that shown in Fig. 2.1. In addition, the DRM19 mechanism also includes the oxidation of hydrogen, but there is no formation or consumption of H_2O_2. The species present in the mechanism are solved throughout the domain of interest, using the boundary and initial conditions given in section 2.1.2.

Note that the numerical performance of the DRM19 was tested against the GRI-Mech for ignition delay and laminar flame speed simulations [49]. The ignition delay was studied for different initial conditions of pressure, fuel-air stoichiometric ratio and temperature, presenting a deviation typically within 6-8% with respect to GRI-Mech 1.2. It was also shown that the accuracy of DRM19 drops at lower temperatures and higher pressures. Regarding the adiabatic flame, the maximum mole fractions of H, OH and CH_3 at 1 atm and 10 atm were also analyzed. The results for both pressures were similar with respect to the peak mole fractions, it is also noted that for the 10 atm results the DRM19 performs better for the lean to stoichiometric mixtures [49]. The adiabatic flame speed was accurately predicted with an error equal to 8% for atmospheric pressure and 11% for 10 atm.

This mechanism was also applied to determine a premixed methane/air flame in heated tubes and the Sandia turbulent flames [50, 51]. Regarding non-premixed flames, the DRM19 was used to model a one-dimensional counter flow and a two-dimensional coflow using a biogas mixture (methane diluted with carbon dioxide) as fuel, and compared against other kinetic mechanisms [52]. Another application was the investigation of the "flame street" phenomenon that presents itself on non-premixed flames in narrow channels, where the flame is divided into small segments. In that case, a methane/oxygen combustion in a micro channel was modeled using DRM19 [53].

To model a reactive flow it is necessary to define, first, some characteristic properties of the flame, e.g., the stoichiometric ratio, the flow regime, the fuel, and if the flame is premixed or not. This requires the selection of the burner, which determines both boundary conditions and flaming regimes. Here, a methane/air laminar non premixed flame stabilized on the Gülder burner is studied. The obtained flames are characterized by well-defined fields which ease the analysis of the properties.

2.1.2
Computational domain and boundary conditions

It is indispensable to define the geometry of the domain of interest and the mesh where the simulation is effected. Thus, here the numerical simulation setup is now given, such as the boundary conditions, and the calculation methods.

The computational domain used to represent the Gülder burner is shown on Fig. 2.2. The dimensions of the fuel and air inlets, and the burner wall thickness are the same as for the burner shown on Fig. 1.1b, radius of 5.5 mm and 43.5 mm for the fuel and air inlets, and a wall thickness of 1 mm. Since the studied flame is axisymmetric, due to the chosen burner characteristics, a two dimensional geometry is used. Figure 2.2 presents a representation of the domain of interest and its boundary conditions, using different colors to represent each of them. The axis of symmetry is the 160 mm length yellow line, the four grey lines represent the walls, the outlet and the two inlets are the red and the blue lines, respectively. There are two types of walls in this domain; the burner wall, which has an adiabatic, non catalytic, no-slip condition, and the one representing the outer boundary, which has a slip and constant temperature condition. The walls between the burner inlets are denominated as burner walls, and the free boundary is the external right boundary, with a length of 150 mm.

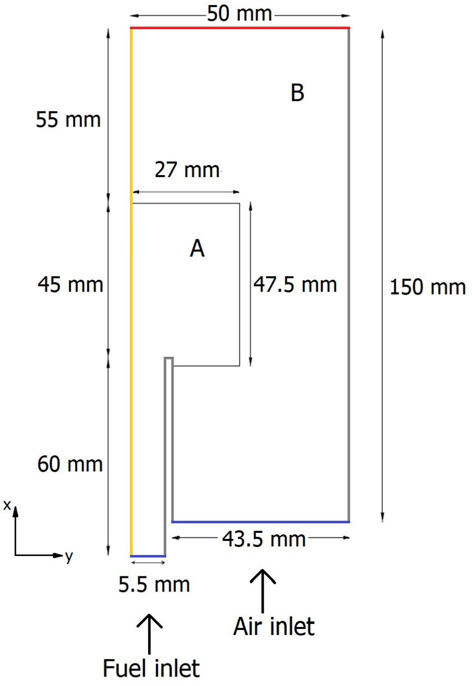

Figure 2.2: Representation of the Gülder burner computational domain and its dimensions. (A): internal part, (B): external part.

The burner was designed to ensure that the flame is laminar, and the fuel flow at the outlet of the fuel tube is hydrodynamically developed. Therefore, the length of the tube is long enough, such that the flow does not vary in its axial direction. Such length for the laminar case is a function of the Reynolds number ($L_e \cong 0.05 D R_e$) [6]. The length of the fuel and air feeding tube are 60 mm and 50 mm, respectively.

As the flame studied is a non premixed flame, air and fuel enter the domain of interest through different inlets, as shown on Fig. 2.2, such that the mixing of reactants only occurs at the reaction zone. Concerning the inflow conditions, at the inlets, the species molar fraction, temperature, pressure and the inlet velocity are given. The air is a mixture composed by 21% O_2 and

79% N_2, and the fuel is methane. Air and fuel have prescribed temperature and pressure of 300 K and 1 atm, respectively.

In this work, the impact of varying the fuel inlet velocity is discussed. A total of 20 different velocity values are considered and simulations are performed for equally spaced within chosen thresholds. Table 2.2 presents the Reynolds number and the Froude number, defined as Fr=$v/\sqrt{\vec{g}D}$, for the fuel velocity thresholds limits. The inlet velocities are chosen according to the experimental study where the air inlet velocity is constant and uniform, $v_{z|a,in}$ =60 cm/s, and the fuel inlet velocity ($v_{z|f,in}$) is uniform and varies between 1.75 and 4.38 cm/s, as shown in Tab. 2.3 [54].

Table 2.2: Prescribed fuel inlet velocity ($v_{z\,|f,in}$), Reynolds number (Re), Froude number (Fr) and computed flame length (L_f) for the lower and higher velocities studied.

$v_{z\,|f,in}$ [cm/s]	Re	Fr	$L_{f,c}$ [cm]
1.75	11.38	0.05	1.42
4.38	28.48	0.13	3.50

Table 2.3: The 20 prescribed fuel inlet velocity ($v_{z\,|f,in}$) studied. The blue colored cases represents the validation cases in the ROM construction presented in Sec. 2.2.

Case	$v_{z|f,in}$ [cm/s]	Case	$v_{z|f,in}$ [cm/s]
1	1.75	**11**	**3.06**
2	1.91	12	3.23
3	**2.08**	**13**	**3.31**
4	2.24	14	3.39
5	2.41	**15**	**3.56**
6	**2.57**	16	3.72
7	**2.65**	17	3.89
8	2.74	**18**	**4.05**
9	**2.90**	19	4.21
10	2.98	20	4.38

The length of the domain, from the burner outlet to the gas exit, is 100 mm, which has been estimated based on the experimental flame height [54]. Table 2.2 gives the computed flame heights for the lowest and highest velocity modeled cases, being smaller than the domain height. The numerical flame height is obtained by determining the distance, between the tube exit and the position of the maximum mass fraction of the H radical along the symmetry axis, i.e., along the centerline of the computational domain.

Although the acceleration of gravity influences the studied flames, as shown in Tab. 2.2 through the Froude number, all cases were solved by neglecting gravity. In other words, since the objective of the work is to use the results obtained through CFD to build ROM, an analysis of a non premixed flame in the absence of gravity is considered only.

For the purpose of meshing, the domain is divided in two parts, the internal part (A) is composed of the central tube, where there is only fuel flow, and the estimated mixture region, where the chemical reactions occur. The external part (B) includes the air entrance and the outlet, in other words, air and burned gases flows only. This division enables the use of different mesh sizes along the domain.

2.1.3
Numerical methods of solution

In this work, the multi-scale problem is solved using the *Ansys* software Fluent 2019 R3, which applies finite volume [7, 45]. Since those methods are quite standard, no further discussion is developed here.

The stiff chemistry solver is used to advance the reaction in the species transport equation, which consists in a fractional step algorithm for pressure-based unsteady simulations [55, 56]. In the first step, the chemistry in each cell is solved at constant pressure for the flow time-step, using the In Situ Adaptive Tabulation technique. Then, the convection and diffusion terms are treated as in a non-reacting simulation. For a pressure based steady case, this method approximates the reaction rate (ω_i) in the species transport equation as [48]:

$$R_i^* = \frac{1}{\tau}\int_0^{\tau} R_i d\tau \qquad (2\text{-}13)$$

where τ is the fictional appropriate time-step, the default being one tenth of the minimum convective or diffusive time-scale in the cell [48]. As τ tends to zero, the approximation becomes exact [48]. On the other hand, as τ tends to infinity, the approximation R_i^* tends to zero, the numerical stiffness (chemical timescales) is alleviated, meaning, no reaction. In this work the configurations used of the stiff chemistry solver are the default and it is applied every iteration.

The detailed chemical kinetics mechanisms contain several intermediate species in addition to the principal species: the fuel, oxidant, and products. Since these intermediate species evolve at very different reaction rates, the time scales for species formation and consumption are different by several orders of magnitude [4]. To accurately determine the species evolution, the numerical time integration requires very small time sub-steps, causing large computational simulation time [48]. One way to speed up this process is through the in-situ adaptive tabulation integration (ISAT) tool [48].

The ISAT has been widely used as an integration method in combustion simulations [57, 58]. It is employed to integrate the stiff chemistry to reduce the burden of a direct integration of the chemistry [57, 48]. The method tabulates the chemistry mappings during the simulations with error control, accelerating the solution time. The numerical error in this dynamical tabulation is controlled by the predefined ISAT error tolerance. Note that the smaller the error tolerance, the higher memory and time required to build the ISAT table [48]. In addition, the performance of ISAT decreases in flames with large time scales, since more work is required on the integrator of the ordinary differential equation [57]. In this work, the ISAT table is used as integration method, and with an error tolerance of 10^{-4}.

2.1.4
Adaptive computational mesh

To properly describe the chemical reaction and all of its scales, a refined mesh is necessary. However, using a refined mesh in the whole computational domain makes the computational cost of the simulations infeasible. To overcome this problem, the domain divided in two parts, thus enabling to decrease the computational cost by defining the refined mesh at the combustion region only, i.e., where it is needed. Since the internal part (A) contains the reactive zone, it has a more refined mesh. Such internal part has a rectangular mesh, with an initial size of 100 μm and 1 mm in the radial and axial directions, respectively. The external part (B) has a uniform mesh with a size of 1 mm. Even though a refined mesh is used at part A, those meshing spacings are not enough to properly compute the combustion scalars, especially the minor species. Therefore, a mesh adaptation tool is used to refine and coarsen the mesh when needed.

The adaptive mesh refinement is usually performed to reduce the numerical error with reduced numerical cost. It is a resource that enables the refinement and/or coarsening of the mesh based on numerical solution data [59, 60]. The purpose is to add mesh cells/nodes where it is necessary, since computational meshing is a rationed resource — especially in 3D cases. Therefore, this enables the flow characteristics to be solved accurately.

Here, the procedure used for the mesh adaptation is the hanging node adaptation [48]. The meshes generated by this method have nodes on edges and faces [48, 59]. This adaptation technique gives the ability to operate on meshes with different cell shapes, including hybrid meshes. For example, in the case of a 2D mesh refinement, a quadrilateral cell is split into four quadrilaterals, as shown in Fig 2.3, whereas 3D case with an original hexahedral cell is divided into eight identical hexahedrons.

One of the controls used in this adaptation is the maximum refinement level, which specifies the maximum number of times the original cell edge can be divided on two new edges [61]. For example, a maximum refinement level of 2 can split a quadrilateral cell up to 16 subcells, as shown on Fig. 2.3. Although the hanging node scheme provides significant mesh flexibility, it requires additional memory to retain the mesh hierarchy used by the mesh rendering and adaptation operations, when compared to a structured mesh [62, 61].

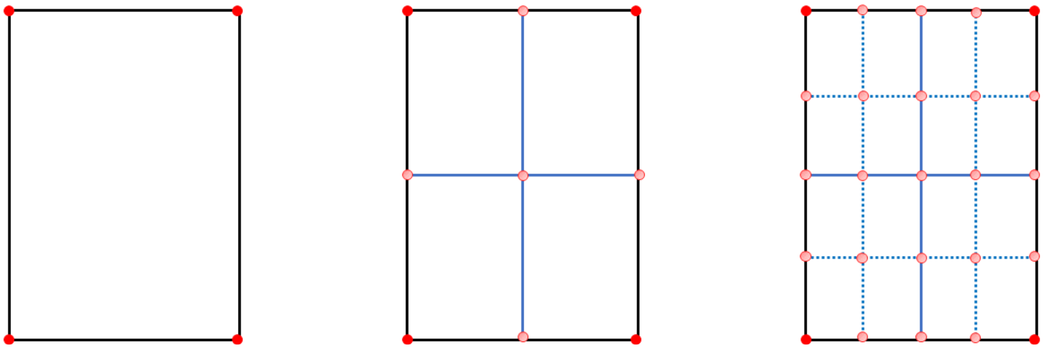

Figure 2.3: Representation of the hanging node adaption for two-dimensional quadrilateral cell. In this adaption, the original cell is divided upon 4^n, where n is the max refinement level. The left square represents the original quadrilateral cell, and the right the cell divided into 16 subcells. Adapted from [48].

Assuming that maximum solution error occurs in high gradients regions, the so-called gradient adaption approach, that is one of the three options available in Fluent, is used. In this approach, the Euclidean norm of the gradient of a defined property is multiplied by a characteristic length scale, i.e., for a two dimensional problem, the gradient function has the form [63, 64]:

$$|e_{i1}| = (A_{cell})^{(r/2)} \left|\nabla f\right|, \tag{2-14}$$

where e_{i1} is the error indicator, A_{cell} is the cell area, r is the gradient volume weight, and ∇f is the Euclidean norm of the gradient of the defined field property f.

In this work, a gradient mesh adaptation based on the temperature is applied, with a refinement and coarsening thresholds of 10 K/m and 300 K/m, respectively. A trial and error procedure, based on the temperature sensitivity test in mesh adaptation and the ignition method [65], was performed to determine the threshold values for the case of the laminar non-premixed flame with the fuel inlet velocity of 17.5 cm/s, and is not shown here for brevity.

The temperature gradient is well known to ensure an appropriate adaptation criterium for combustion systems [49]. In this work, an adaptation based on a single property, temperature, is done every 25 iterations. As an example of the use of such an adaption procedure, for the case of $v_{z|f,in} = 4.38$ cm/s, the initial mesh has 11,667 nodes, and in the end of the simulation it has 93,168 nodes, i.e., 81,501 nodes more than the original mesh.

Ignition of the reactive simulation is performed using a high-temperature region, combined with the adaptive mesh procedure. Departing from a converged isothermal simulation result, a patch of 3 mm in the radial and 5 mm in the axial direction is set at the stoichiometric line ($Y_{CH_4,st} = 0.055$) 1 mm above the fuel feed tube outlet. This patch is initialized with a temperature of 1,800 K, which is the methane adiabatic flame temperature. Once this reactive simulation converges, the temperature field obtained is used as, in the remaining reactive simulations, as ignition trigger.

2.2
Reduced order model

In order to obtain high-fidelity CFD simulations, there is a high computational cost, especially in relation to memory and simulation time, which often makes a parametric study unfeasible. Therefore, machine learning techniques, such as reduced order models, have been applied to overcome this shortcoming [21, 28].

Reduced order models enables a simple representation of complex systems, without losing the main characteristics of those [25, 77, 21]. In this work, a software is used to create ROM for combustion, called the *Static ROM* of *Twin Builder* from *Ansys*, as shown in Fig. 2.4. Its construction is divided in four steps; (1) choosing the learning dataset, (2) decomposing the data in simplified form, (3) retaining the main characteristics of the learning set and (4) applying a machine learning interpolation.

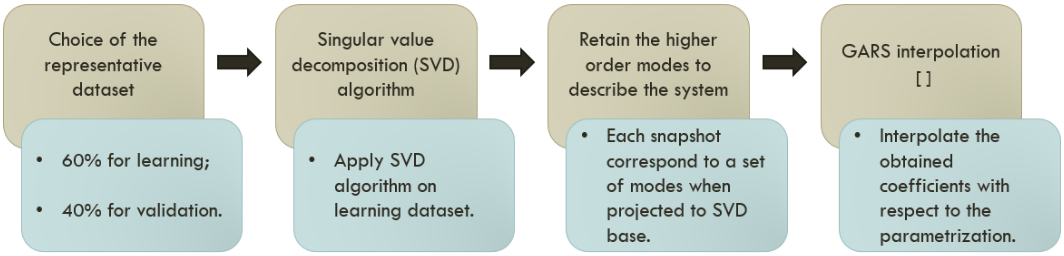

Figure 2.4: Scheme of the procedure for constructing reduced order models for static systems (Static ROM).

The first step consists on obtaining representative data of the system of interest, of which 60% is used to learn the model, and the remaining 40% to its validation. One may note that the learning set must include the extremes of the parametric space, in order to avoid an extrapolation when the obtained ROM is used. In the second step, a singular value decomposition (SVD) is applied to decompose and obtain the system modes. The SVD organizes the modes in decreasing order, such that the higher mode values retain the most important characteristics of the system of interest. At the third step, the decomposed system is filtered, retaining only the most important characteristics, i.e., the higher order modes. This procedure generates a reduced base which is used to describes the entire system [66]. The accuracy of the ROM is influenced by several factors, for example, the data available, the number of modes used on the reduction of the learning set, and the interpolation method error [23].

Finally, the interpolation is performed with Genetic Aggregation Response Surface (GARS), which applies a selection process to determine what type of response surface (RS) better describes the system [67, 68]. Since GARS can be defined as a weighted average of a set of response surfaces, and has a cross-validation process, where the risk of an algorithm spreading the data set is estimated, this method presents an improved reliability when compared to other classical response surface [67, 69]. A reduced model is then created to describe the behavior of the studied system, for an arbitrary value of the variable parameter. Then, the prediction of the validation data may be performed. Following, a brief description of the methodologies involved on the ROM is presented.

2.2.1
Singular value decomposition

The singular value decomposition of a matrix is the factoring of a real, or complex, matrix into three matrices U, Σ and V^T [66]. The SVD takes a high-dimensional data and transforms it into key features of that data. This decomposition has many different applications, for instance, in signal processing and statistics, in recommender systems and in algorithms for facial recognition [24].

Figure 2.5 shows a scheme of the data matrix $\mathbf{A}$, used to create the reduced order model, its decomposition and reduction. The columns are the cases modeled separated as learning data, and the rows are the information of each cell of the domain. Note that the data provided to create the ROM has the same number of rows, which means that even though CFD simulations use adaptive meshing, the data provided to the ROM is extracted from a uniform mesh. To do that, the converged results for each fuel inlet velocity are interpolated on the uniform initial mesh and then extracted, in order to create a dataset to build the ROM. Note that this procedure degrades the accuracy of the obtained results.

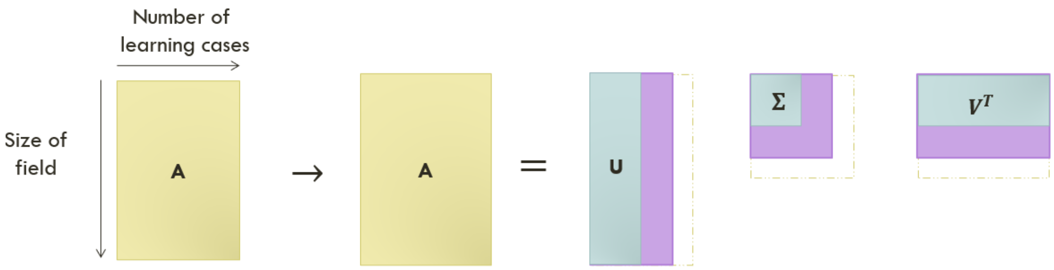

Figure 2.5: Scheme of the singular value decomposition to build a basis of vectors representative of any system.

Regarding the decomposition properties, U and V are unitary matrices and known as left and right singular vectors, respectively. The Σ matrix is diagonal with non negative numbers hierarchically ordered, called as singular values. Since those are ordered in terms of importance, it is possible to ignore the smaller singular values and approximate the matrix $\mathbf{A}$ only in terms of the first few dominants columns [66]. Assuming that the number of rows is much larger than the number of columns, restricting the number of non zero singular values, as there are only m linearly independent rows and columns of the data matrix $\mathbf{A}$ [24, 66].

One may note that the SVD reduction process does not find the exact data matrix $\mathbf{A}$, but approximate one. The truncation of SVD is interesting because it is economical to describe the data present in the matrix $\mathbf{A}$ using as few modes as possible from the columns of U and V. In Fig. 2.5, the SVD matrices presents three different colors, representing two different reductions. It is possible to see that as the amount of modes increases a more accurate, but more complex, model is found [66].

2.2.2
Genetic aggregation response surface (GARS)

In this work, the fourth step of the ROM construction, as seen in the schematic of Fig. 2.4, is the GARS interpolation method discussed above. It is constructed using four different integration methods [68, 70]; polynomial regression, Kriging, support vector regression and moving least squares [71, 72, 73, 74]. Here, the GARS uses a selection process to determine the combination of response surface (RS) that best describes the system, which, in this work, are the flame properties fields.

The genetic aggregation algorithms (GA) are based on the principle of natural selection, which means that it improves the population from generation to generation, making the algorithm more effective [24, 69]. To achieve this improved algorithm, different process are used, such as crossover, mutation or replication [67]. Nevertheless, the Genetic Aggregation Response Surface (GARS) is a method based on GA algorithms using different response surface methods as population, e.g., full second order polynomial, kriging, neural network [75, 76].

This method was used, for instance, to analyze the pressure and strain fields to study the formation of pressure ulcers and to create a real-time model to prevent pressure ulcers in the sitting position [77]. Furthermore, it was applied to investigate the configuration of the parameters of single-wound heat exchangers, aiming to determine the optimal configuration [69].

In order to preserve the accuracy of the RS on the design points and its stability, a universal criterion consisting of a three components measuring model quality; cross-validation, internal accuracy on the design points, and a roughness penalty was proposed [68, 67]. So, based on this criterion a surrogate model selection algorithm known as the Genetic Aggregation using a penalized predictive score (PPS) has been proposed [75];

$$\widehat{A}_m(x) = \sum_{l=1}^{m} \omega_l \hat{s}^{(l)}(x), \tag{2-15}$$

where, $\widehat{A}_m$ represents the aggregation of m surrogate models ($\hat{s}$) weighed by ω_l, which is calculated using the PPS method. The genetic aggregation algorithm is applied in the reduced base to create a model that describes the system behavior for an arbitrary value of the variable parameter. In the present work, the variable parameter is the fuel velocity.

It is worth to note that, in combustion problems, it is important to account for of some physical restrictions. More specifically, with respect to the combustion scalars, monotonicity, positivity, and boundedness are critical properties [44, 45]. Note also, that other problems, such as bankruptcy predictions, or medical diagnosis that use machine learning algorithms, also have to be concerned with monotonicity restrictions [78]. Therefore, a ROM methodology for describing these problems has to guarantee these three properties.

In the case of interpolations used for the discretization of conservation equations, high-order accuracy methods are known to enforce these properties, such as weighted-essentially-non-oscillatory (WENO) and total variation diminishing (TVD) [79, 80]. However, the methods used in GARS are not monotonicity preserving [71, 72, 73, 74]. As a consequence, the reduced order model here obtained are not expected to enforce these three properties.

2.3
ROM application

In this work, the fields of 23 properties (temperature; velocity components and the species mass fraction, except for the activated CH_2^*) for each fuel inlet velocity modeled with CFD are used to create the reduced order model representative dataset of the methane/air laminar non-premixed flame.

However, when performing the ROM of this flame an issue related to the monotonicity of the combustion properties obtained has been observed, this will be further detailed in chapter 3. To overcome this problem, different methodologies are proposed to pre-process the available data, which are presented in the following.

2.3.1
Learning data pre-process

It is well known that the data provided for learning has a remarkable impact on the model prediction. As a consequence, knowing its main characteristics is important to achieve a representative ROM. For that, data processing tools should be used to give insights thus, facilitating the learning process.

Here, the methodologies applied to pre-process the CFD data in different ways are discussed. First, a methodology regarding the properties being treated as uncoupled or a coupled system in the construction of the ROM is presented. Indeed, since in the combustion process all the flame properties are closely coupled through the chemical reaction, is interesting to study the effect of coupling (or not) these properties to construct the ROM, thus, considering it a single system.

Figure 2.6 presents two schemes that represents the uncoupled and coupled methodology. In this figure, there are 5 properties (A, B, C, D and E). For the uncoupled methodology, Fig. 2.6a, each property has their respective ROM, that means that property A data only influences itself and its reduced order model. On the other hand, the coupled methodology, Fig. 2.6b, has only one reduced order model, created using the data of all 5 properties, such that all properties impact each other.

By coupling the properties, an information concerning the system studied is considered. In other words, as in the combustion process, the result of the coupled ROM is influenced by all the properties, which is not the case for the uncoupled ROM. Thus, it is expected that the result is more faithful to the one obtained by CFD, than the uncoupled ROM results.

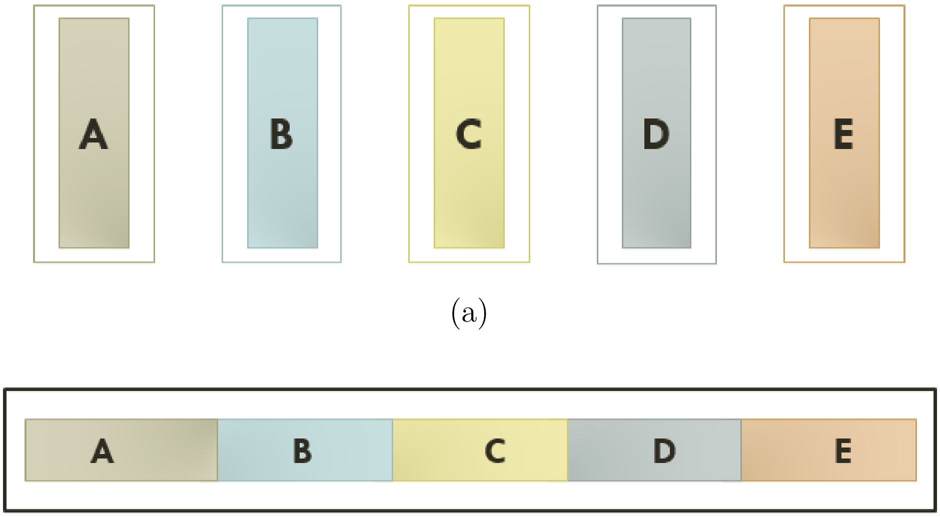

(a)

(b)

Figure 2.6: Uncoupled (a) and coupled (b) ROM scheme.

Moreover, willing to facilitate data learning process even more the ROM, other pre-processing methodologies are applied to the data. More specifically, two other methodologies are applied to the learning dataset: (i) the normalization of the properties, and (ii) the logarithm of the chemical species. Following, these methodologies are presented.

Normalization of properties

Each of the 23 transported properties have values that differs in several orders of magnitude. For example, the maximum temperature reaches about 2,100 K and the minor chemical species, such as the CH_2 radical, have a maximum mass fraction of $3 \cdot 10^{-5}$. This should be taken into account when coupling the properties, because the singular values are sorted in hierarchical order, which implies that quite small values can be ignored in order to approximate the matrix only on the first dominant terms. Therefore, the effect of normalizing the data must be studied, and this pre processing is widely used in other problems using machine learning or system identification techniques [24, 29, 25].

Therefore, the normalization goal is to change the different data values to a common scale, without biasing the differences in the value ranges. As the studied flame is multi-scale, the impact of the normalization of temperature, velocity components, and species are investigated such that:

$$T^* = \frac{T(k) - T_0}{T_{ad} - T_0}, \quad u^* = \frac{u(k)}{u_{max}}, \quad u_{max} = u_0 \frac{T_{ad}}{T_0}, \quad Y_i^* = \frac{Y_i(k)}{Y_{i,max}}, \tag{2-16}$$

where T^*, u^* and Y_i^* are the normalized temperature, velocity component and species i mass fraction. T_0 is the temperature of fresh gas, 300 K; T_{ad} is the adiabatic flame temperature of stoichiometric methane/air mixtures, 2,236 K; u_0 is the air inlet velocity, 60 cm/s, and $Y_{i,max}$ is the maximum concentration of the species i found when the CFD simulation converges.

One may note that, to estimate the temperature and velocity bounds in the reactive case, the reference temperature in the chemical equilibrium (T_{ad}) and the velocity are known. However, each chemical species maximum concentration is unknown a priori, since they depend on the process details. Thus, the estimation of a reference for these parameters is not straightforward. To understand the influence of normalization, a reduced order model using the properties coupled (1) without the normalization, (2) with the normalization of temperature and velocity, and (3) with all properties normalized are studied.

Logarithm of species

The application of the logarithm to the computed species mass fractions reactions is proposed based on previous knowledge of classical combustion systems. Indeed, the spatial decrease of the mass fractions due to diffusion and convection process is exponential [4].

In order to avoid applying the logarithm in regions where chemical species are absent, a truncation parameter (ϵ_c) is imposed on the mass fractions data. Then, the log_{10} is applied to the data set before the ROM construction, i.e.,

$$\hat{Y}_i = max(Y_t, 10^{-\epsilon_c}). \tag{2-17}$$

$$\bar{Y}_i = \log_{10}\left(\hat{Y}_i\right). \tag{2-18}$$

This set of operations is performed for all the chemical species, for each fuel input velocity modeled. After the learning process the results obtained with the ROM (for the validation cases) are exponentiated, so as to recover is Y_i. Then, these results are interpolated on the uniform mesh, analyzed and compared with the other pre-processing results. In addition, a study of the influence of the parameter ϵ_c on the final result is performed also. This is effected by analyzing the reconstructed mass fractions and the influence on the singular values, in order to determine the value of the truncation parameter that best suits all species reconstruction. The three truncation parameter values chosen are 8, 10 and 12, which are all smaller than the maximum mass fractions found for the minor species.

2.3.2
ROM nomenclature

As different methodologies for pre-processing the properties data are considered, a nomenclature is suggested to synthesize the construction information from each ROM. The nomenclature chosen to classify the reduced order models studied summarizes the main information regarding the data pre-processing and the ROM construction. It states, for example, the methodologies applied to the learning data, such as normalization or logarithm, whether the ROM has uncoupled or coupled combustion properties, the number of learning cases, and the number of modes used. The nomenclature is given as:

$$ROM_{(i,j)}^{(c|m|p)}, \tag{2-19}$$

where the subscript (i, j) refers to the number of learning cases and the number of modes, respectively; and the superscript $(c|m|p)$ refers to the data organization:

- the first item, c, states if the combustion properties are treated as an uncoupled (u) or a coupled (c) system;
- the second, m, refers to the methodology applied to the learning data. Table 2.4 relates the studied methodologies to the symbols used in the nomenclature.
- the last item, p, is the specific property studied, for example: v_x and v_y for the axial and radial velocity or T for the temperature.

Table 2.4: Methodologies applied to the learning data and its symbols.

methodology	symbol
without normalization	w
normalization of temperature and velocity	$n_{t,v}$
normalization of all properties	n_{all}
logarithm of species	l

In the case of the coupled ROM, a slightly different nomenclature is used (pc, ps). Meaning that first is stated that the properties that are coupled, and then the property of interest. For example; the result of OH mass fraction obtained by the reduced order model using 12 learning cases and 5 modes, with all properties normalized and coupled, is denoted:

$$ROM_{(12,5)}^{(c \ | \ n_{all} \ | \ all,OH)}.$$

3
Results and discussion

In this chapter, the results obtained are presented and discussed. Firstly, those corresponding to the use of CFD are introduced, with the aim of describing the structure of the methane/air flame by means of twelve different flame properties. Then, the results of different created ROM are analyzed, beginning with a data decomposition analysis and, then, comparing different ROM predictions, for each applied method, with the CFD data.

It should be stressed that each CFD computation required around 15 days to reach convergence, using 18 cores of a 24 CPU in a computer with 32 GB of memory using Windows 10. The processor is the AMD Ryzen 9 3900X 12-core, running at 3.79GHz. The software used was Ansys Fluent, version 2020 R2, for flow analysis and flame calculation, and static ROM from Ansys Twin Builder, version 2020 R1, to create the ROM.

The exact solution to an iterative problem, such as the CFD simulation is unknown, however, one aims to be sufficiently close to the exact solution for a desired accuracy. There are several approaches to verify the convergence of numerical problems, such as the residue curve or the Richardson extrapolation [81]. In this work, the approach based on the observation of minor variations in different properties along the CFD iterations is adopted. Due to the adaptive meshing process, the upstream adaptation interferes in the downstream outcome. So to verify the necessity to further mesh refinement, at each mesh adaptation the variations in the temperature and the OH radical, CO and CH_2 radical mass fractions fields were observed. When a sufficiently refined mesh is reached, the simulations proceed without the adaptation while expecting to converge. This convergence verification is done by checking the profile of CH_2 radical, because, in addition to being a minor species, it has a thinner and longer distribution when compared to OH or CH_3 radicals. Furthermore, each simulated case involves a total of 252,200 iterations.

3.1
Non premixed flame structure

In order to discuss the influence the fuel flow Reynolds number, Fig. 3.1 shows a qualitative comparison of the classic flame structure at the extremes of the studied velocity range, where the lowest velocity appears on the left and the highest velocity on the right. The first figures (3.1a, 3.1b and 3.1c) present the velocity components and the temperature, whereas the remaining figures (3.1d, 3.1e and 3.1f) reproduce the mass fraction field of three chemical species: OH, CH_2 radicals and CO. Those have been chosen to represent intermediate species with different length scales.

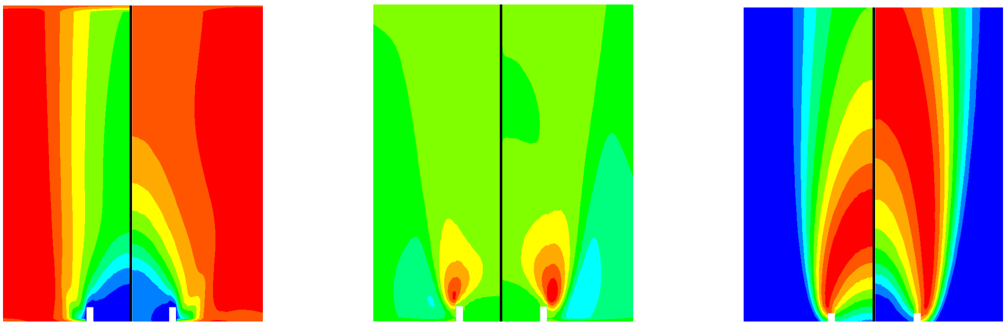

(a) v_x. (b) v_y. (c) T.

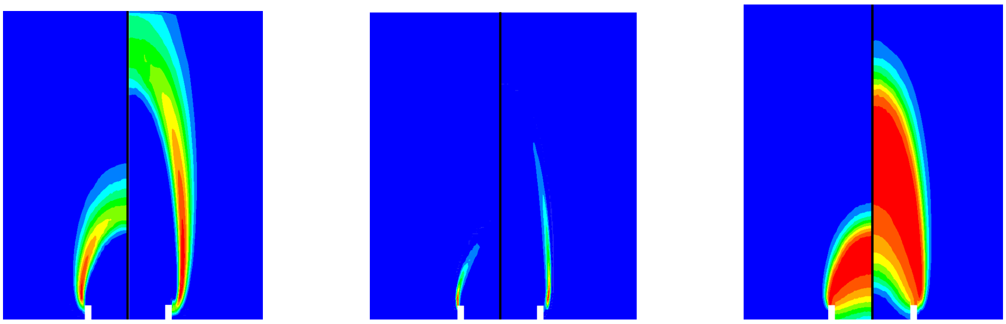

(d) Y_{OH}. (e) Y_{CH_2}. (f) Y_{CO}.

Figure 3.1: Comparison between the flame structures obtained with CFD for the lower (left), $v_{z|f,in} = 1.75$ cm/s, and higher (right), $v_{z|f,in} = 4.38$ cm/s, prescribed fuel inlet velocity. The color map limits are $v_x \in [0,\ 67.7]$ cm/s; $v_y \in [-17.2,\ 17.2]$ cm/s; $T \in [300, 2, 158]$ K; $Y_{OH} \in [0,\ 3.89 \cdot 10^{-3}]$; $Y_{CH_2} \in [0,\ 2.67 \cdot 10^{-5}]$; $Y_{CO} \in [0,\ 5.11 \cdot 10^{-2}]$. The color map goes from blue (minimum) to red (maximum). The fuel and air inlets are limited by the white rectangle at the lower most part of the images.

The axial and radial components of the velocity field are shown in Figs. 3.1a and 3.1b, respectively. One may note that along the flame, the axial component of the velocity, v_x, increases as it gets further away from the fuel tube exit. This behavior is explained by the increasing temperature, as shown in Fig. 3.1c, which affects the density within the reaction zone. Indeed, based on the conservation of the total mass equation [Eq. (2-2)] and the perfect gas equation of state [Eq. (2-12)]: as the temperature increases, the velocity increases. As for the radial component, v_y, most of the domain (fuel inlet tube and the regions far from the flame front) is green for both the lowest and highest fuel velocities, meaning that the velocity is close to zero, as expected according to mass conservation. Specifically, within the fuel feed tube, from the differential equation of continuity [Eq.(2-5)] considering the hypotheses of steady state, two-dimensional and incompressible fluid, once the flow becomes fully developed, the velocity no longer varies in the x direction. Since the velocity at the wall is zero, the radial component of the velocity is zero when the flow becomes fully developed [7]. However, when comparing the two cases, the region of positive radial velocity is larger for the case of $v_{z|f,in} = 4.38$ cm/s, Fig. 3.1b (right). This larger v_y value is associated to the corresponding larger $\partial v_x/\partial x$.

Examining the temperature profile, Fig. 3.1c, a high temperature region is seen, representing the flame region. The maximum temperature is $2,138$ K for the slowest fuel inlet velocity (left), and for the largest velocity (right) is $2,153$ K, both which are close to the adiabatic flame temperature for methane ($2,236$ K). Downstream the maximum temperature, a temperature decrease is observed along the y axis, due to the combustion products mixture with air, which is at 300 K. As expected, the fuel inlet velocity has a significant influence on the flame, as seen when comparing both temperature profiles (left and right). Indeed, as the fuel inlet velocity increases, the flame lengthens. Moreover, at the lowest fuel velocity case, there is a region within the fuel tube that has a temperature greater than 300 K, which means that the unreacted fuel is being preheated by the flame via heat conduction when the lowest velocity is considered.

Figures 3.1d, 3.1e and 3.1f show the mass fraction fields of hydroxyl radical (OH), carbon monoxide (CO) and methylene radical (CH_2), respectively. The position and shape of the flame are often estimated using the OH mass fraction profile. The highest concentration of OH is present near the tube walls for both inlet velocity values. However, for the higher fuel velocity, the region of maximum OH concentration and, thus, the flame height are longer. Note that the OH concentration along the streamwise direction decreases due to the progressive dilution by combustion products. This is observed for all intermediate species. Furthermore, carbon monoxide is present within the flame region, and for the case of lower fuel velocity, CO is found within the fuel inlet tube also. Such a mass diffusion phenomena is associated to the increase on the fuel temperature inside the tube, seen in Fig. 3.1c. It is worth to note that, for the higher velocity case (right), the region of maximum concentration of this chemical species is wider than the region found for the lower fuel velocity case (left).

Regarding the mass fraction field of CH_2 radical, Fig. 3.1e, a mass fraction of the order of 10 *ppm* is seen, and the region where CH_2 is present is quite narrow, approximately 500 μm. One may note that this species is the one with the smallest time and length scales, being quickly created and consumed within the reactive region, and thus is an effective indicator of the flame front position [37]. The maximum concentration is located near the burner wall, and for the lowest fuel inlet velocity case is 29 *ppm*. Note that this property was used as the convergence parameter, i.e., when the field of the mass fraction of CH_2 stops varying, all other variables are assumed to be converged.

A total of 23 flame properties are obtained from the CFD simulations: the velocity components, temperature, and the 20 chemical species present in the DRM19 mechanism. Although some of these species qualitatively resemble each other, for the sake of completeness it is interesting to analyze more than three species, and at an intermediate fuel inlet velocity value, since there is a large influence of the fuel inlet velocity on the flame, as seen in Fig. 3.1. In addition, the species concentration spare over sever orders of magnitude, and arise at different locations during the combustion process.

Therefore, in order to characterize the flame, and subsequently compare qualitatively with the results obtained from the reduced order models, in the interest of brevity, twelve flame properties are analyzed throughout of this work, as shown in Fig. 3.2. As in the following section these twelve properties are compared with the ROM results. The fuel inlet velocity chosen represents one of the validation cases, i.e., cases that are not used in the construction of the reduced model. The first three of these properties are the axial and radial components of velocity and the temperature, Figs. 3.2a - 3.2c, respectively. Then, the mass fractions of H, OH and HO_2 radicals, Figs. 3.2d - 3.2f are respectively given, which are related to the hydrogen oxidation mechanism. Finally, Figs. 3.2g - 3.2l present the species encountered in the oxidation of methane, and those are: CH_4, CH_3 radical, CH_2 radical, CH_2O, HCO radical, and CO respectively.

The chosen species represent the different mass fraction scales and their different profiles, representative of the major, intermediate and minor species involved on the combustion process. One should also note that five of those species (CH_4, CH_3, CH_2O, HCO, and CO) are in the central path of the methane oxidation chain, in Fig. 2.1. The CH_2 is a minority species that is of significant importance as an intermediate species, which is rapidly consumed, as on the diagram in Fig. 2.1. The CH_2 pathway is the second most important in the decomposition of CH_3 and the formation of HCO, as may be seen in that figure.

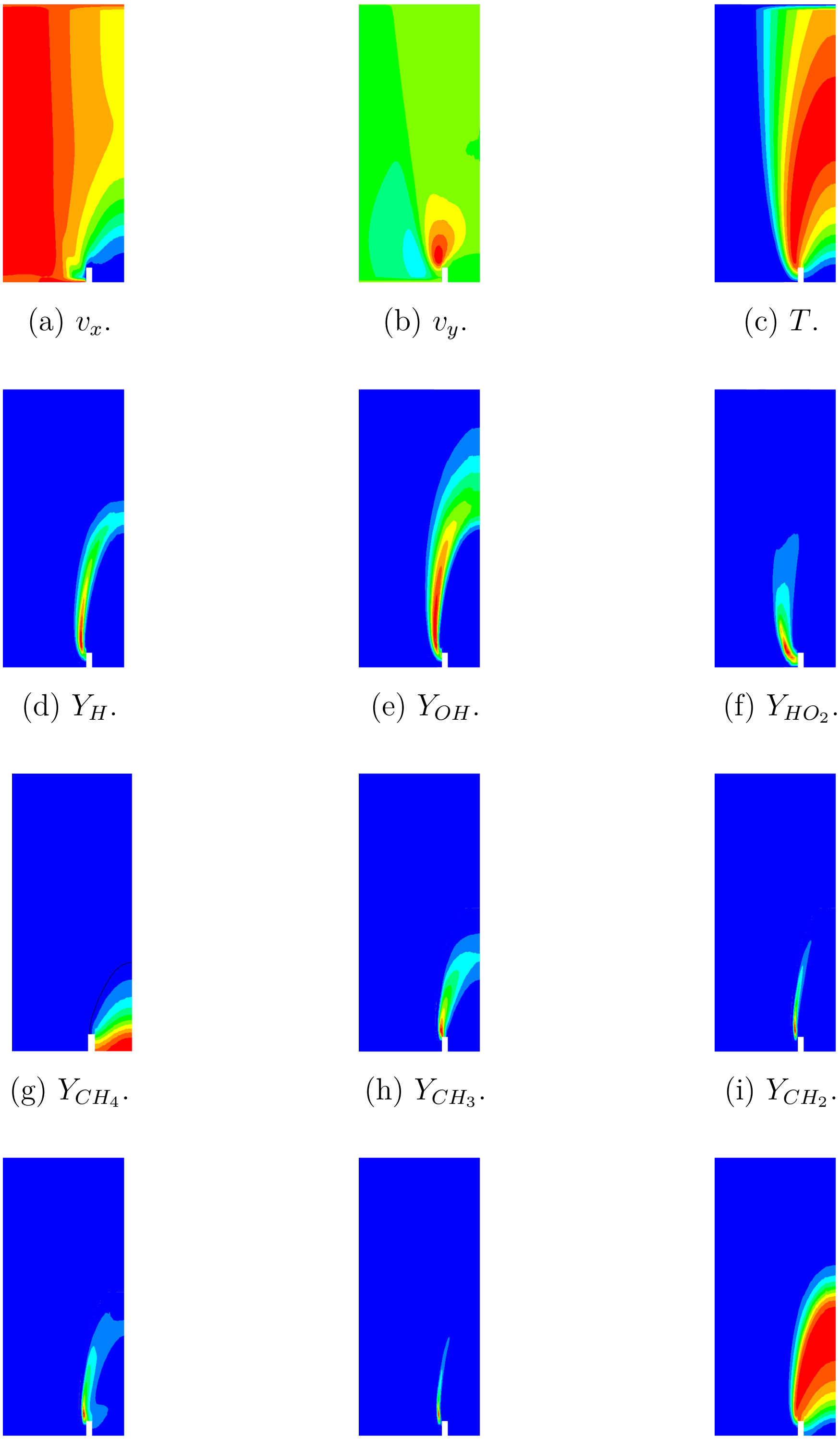

(a) v_x.

(b) v_y.

(c) T.

(d) Y_H.

(e) Y_{OH}.

(f) Y_{HO_2}.

(g) Y_{CH_4}.

(h) Y_{CH_3}.

(i) Y_{CH_2}.

(j) Y_{CH_2O}.

(k) Y_{HCO}.

(l) Y_{CO}.

Figure 3.2: Flame properties obtained with computational fluid dynamics (CFD) for the validation case with prescribed fuel inlet velocity of $v_{z|f,in} = 3.1$ cm/s. The color map limits are $v_x \in [0, 67.7]$ cm/s; $v_y \in [-17,\ 17]$ cm/s; $T \in [300,\ 2,151]$ K. $Y_H \in [0,\ 1.1 \cdot 10^{-4}]$; $Y_{OH} \in [0,\ 3.9 \cdot 10^{-3}]$; $Y_{HO_2} \in [0,\ 2.3 \cdot 10^{-5}]$; $Y_{CH_4} \in [0,\ 1]$; $Y_{CH_3} \in [0,\ 1.2 \cdot 10^{-3}]$; $Y_{CH_2} \in [0,\ 2.8 \cdot 10^{-5}]$; $Y_{CH_2O} \in [0,\ 1.13 \cdot 10^{-4}]$; $Y_{HCO} \in [0,\ 5.1 \cdot 10^{-6}]$; $Y_{CO} \in [0,\ 5.1 \cdot 10^{-2}]$. The color map goes from blue (minimum) to red (maximum). The fuel inlet is located at the bottom right side, and at the left side is the air inlet.

In Figure 3.2a, the axial velocity increases along the symmetry axis, and the highest velocity in the profile corresponds to the air flow. Figure 3.2b shows the radial velocity, where most of the domain is green, i.e., the radial velocity is zero. Also, there are two non-zero regions, one positive and one negative, which accounts for the mixing of the reactants downstream the fuel supply tube. Those velocity components are qualitative similar to those given in Fig. 3.1.

The temperature field, Fig. 3.2c, presents an increase along the x axis from the exit of the fuel supply tube until it reaches the maximum temperature of 2,151 K. Then, the temperature starts to decrease, but it remains higher than the temperature of fresh gases (300 K). This is due to the diffusion of the burned gases and mixing of these gases with the unreacted air. It is worth to note that a high temperature region inside the tube is not seen, as it occurs in the lower velocity case, given in Fig. 3.1c.

Regarding the species involved in the hydrogen oxidation, Fig. 3.2d and Fig. 3.2e show that the intermediate mass fractions of H and OH, respectively, have a similar spatial distribution. Both species have a maximum concentration near the anchoring region, at the air-side burner wall, and exhibit a local maximum at the symmetry axis. The air and fuel side refer to the reactant inlets, being limited by the burner wall, which has a thickness of 1 mm (represented by the white rectangle at the lowest part of the Fig. 3.2). It should be stressed that this 1 mm white rectangle should be used to provide a scaling reference to the dimensions of all figures that exhibit properties fields. The air side is located at the left bottom and the fuel side at the right bottom parts of those figures. However, the OH mass fraction field has a longer region of high concentration, and also it is more spread out along the axis of symmetry than the other hydrogenated species. With respect to the maximum mass fraction, the hydrogen atom H is of the order of magnitude of 10^{-4}, and the hydroxyl, OH, is of the order of 10^{-3}.

The mass fraction of HO_2, Fig. 3.2f, on the other hand, has a maximum mass fraction of 10^{-5}, and it is thus considered a minor species. The mass fraction field of HO_2 is shorter and does not seem to exhibit a local maximum at the symmetry axis. The region of maximum concentration is also smaller (3 mm) and lies close to the anchoring region. Among the species derived from hydrogen oxidation, the HO_2 mass fraction has the anchoring region located in the 2 mm prior to the fuel feeding tube outlet, having a slightly larger anchoring region when compared to the other species. One may note that these three species (H, OH and HO_2) have an anchoring at the air side.

As the studied flame is non-premixed, in the fuel feed tube only the chosen fuel, methane, is found, as shown in Fig. 3.2g. One may note that near the end of the feed tube the methane concentration starts to decrease until it is completely consumed. The black line on Fig. 3.2g represents the stoichiometric surface for the methane/air mixture.

The CH_3 species is the first to be formed in the oxidation of methane, as shown in Fig. 2.1. The mass fraction field of CH_3 is presented on Fig. 3.2h, where qualitative similarities to the profile of H and OH mass fraction can be seen. Nevertheless, the maximum concentration of CH_3 is located at the burner wall, and also exhibits a local maximum at the symmetry axis. However, the CH_3 characteristic length is considerably smaller than H and OH, which is explained because it is an intermediate species and is completely consumed at the very beginning of the methane oxidation path. Note that the stoichiometric surface is located around the middle of the CH_3 profile. Comparing the mass fractions of CH_4 and CH_3, which are of the order of 1 and 10^{-3}, respectively, one may note that methane is a major species, and CH_3 as a minor one.

The CH_2 mass fraction field, depicted at Fig. 3.2i, is characterized by being thin (0.8 mm at 1 mm after the fuel feeding tube outlet) and long, having a maximum near the anchoring region at the air side. Note that, besides the anchoring, the CH_2 field is closer to the air side than to the fuel side, in comparison to the CH_3 and CO mass fraction fields. This species is one of the minor species, with a maximum mass fraction of the order of 10^{-5}. Moreover, the CH_2O mass fraction field, given in Fig. 3.2j, is also located close to the air side, and, in contrast to CH_2, the profile is more spread out. Regarding the order of magnitude, such species is considered to be minor intermediates, having a maximum mass fraction of 10^{-4}.

The HCO mass fraction field, which may be seen at Fig. 3.2k, highly resembles the CH_2 profile (Fig. 3.2i), with a thin outline and located mainly at the air side. In addition, it is also a minor species, with a maximum mass fraction of $5 \cdot 10^{-6}$. Moreover, a small difference on the characteristic length of the field is seen, such that the HCO is shorter than the CH_2.

The last property to be analyzed is the mass fraction of carbon monoxide, given in Fig. 3.2l. Unlike the other species produced from methane oxidation, CO shows a maximum concentration along the inner region of the flame, and not at the flame front. First, the concentration of this species increases along the axis of symmetry and, as it is consumed, the concentration decreases. One may note that, as in the temperature profile (Fig. 3.2c) there is no CO inside the fuel feeding tube, such as was the case for the $v_{z|f,in}$ of 2.11 cm/s, shown in Fig. 3.1f. Regarding the maximum concentration of CO, on the order of magnitude of 10^{-2}, it may be considered a major species.

Finally, it should be emphasized that the same properties and the same representation of Fig. 3.2 will be adopted herein to describe the results of the different ROM. However, for the sake of brevity, a repetition of the flame properties distribution will be avoided whenever it is possible.

3.2
Reduced order models

The data used to construct the different ROM is taken from the 20 reactive CFD simulations, where only the fuel input velocity varies. From each CFD case, a total of 23 property fields are extracted to build the data set. Depending on the methodology applied in learning data pre-processing step, discussed in section 2.3.1, these properties are treated either separately or as a coupled system. Since it has been decided to use 60% of the CFD cases as learning data, 12 of the 20 numerical simulations are randomly separated to construct the reduced order model, so that all ROM have the same learning cases. For the purpose of comparing the results the ROM, as well as the use of the same learning cases, the same number of modes, five, is also used. Then, from a total of 8 validation cases, only three velocities values, 2.1, 3.1, and 4.1 cm/s, are selected to reconstruct the property profiles using the ROM methodology.

Here it is presented the analysis regarding the data decomposition and the reconstruction of 12 flame properties, for all reduced order models created. First, it is analyzed the uncoupled methodology results, followed by the coupled ones. Then, are presented the results of the logarithm pre-processing methodology. For sake of brevity, the data for the velocity of 3.1 cm/s is exposed and discussed in depth only.

3.2.1
Uncoupled properties

In order to study the influence of varying the number of modes on the precision of the reduced order model, Fig. 3.3 presents the singular values of the decoupled ROMs, for five different flame properties. For the sake of brevity, OH, CH_2 and CO_2 mass fractions, temperature, and radial velocity are shown only. The y axis displays the singular values normalized by the sum in a log_{10} scale, and the x axis, the number of modes. The logarithm scale has been chosen to underscore the order of magnitude variations of the singular values computed.

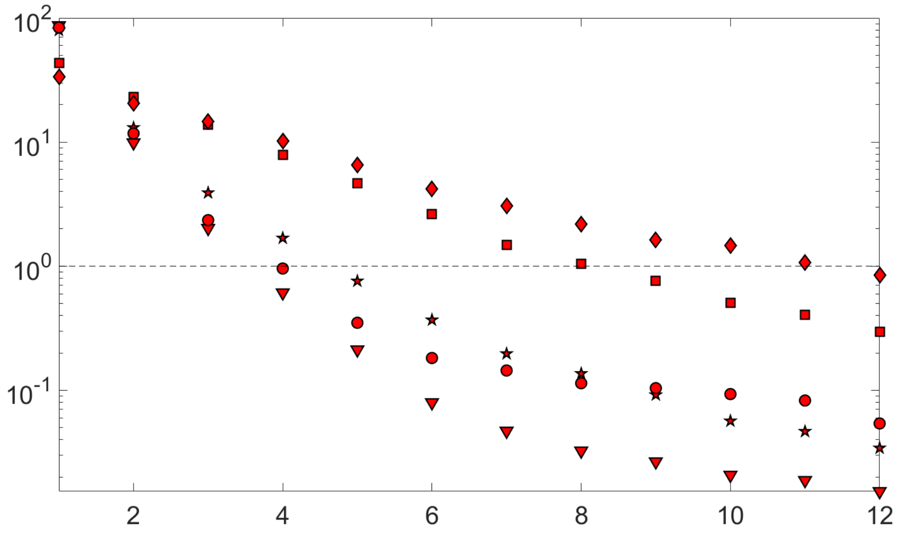

Figure 3.3: Singular values, normalized by the sum, as a function of the number of modes for five properties of the $ROM^{(u|w|p)}_{(12,5)}$. The y axis is represented in a logarithm with base 10 scale and the x axis is a linear scale. ●: v_y; ▼: T; ■: Y_{OH}; ♦: Y_{CH_2}; ★: Y_{CO_2}.

In a general overview, all properties show a similar behavior; by construction, the first modes have higher singular values and, as the number of modes increases, the singular value decreases. This is a feature of the SVD decomposition, where the singular values are ordered in a decreasing value, such that that the information given by first modes retains the main characteristics of the considered system. It is worth to note that for temperature, radial velocity and CO_2 mass fraction, the decrease is steeper than for the OH and CH_2 mass fractions. This becomes clear by tracing a horizontal line at $y = 10^0$ and examining the number of modes the singular value is below the line. For instance, the temperature, radial velocity and CO_2 with five modes, all are below this line. However, for OH and CH_2 this is only observed at the ninth and twelfth modes, respectively. This underscores that learning these flame properties is harder than the velocity components or temperature.

The reconstruction of the $ROM^{(u|w|p)}_{(12,5)}$ flame properties fields is shown in Fig. 3.4. These fields are now compared to those obtained with CFD, the validation data, given in Fig. 3.2. Concerning the axial velocity component, given in Fig. 3.4a, it may noticed that the ROM prediction has a pronounced local minimum at the vicinity of the symmetry axis, in one region with constant velocity represented by the yellow color. However, in the CFD case (Fig. 3.2a) there is only a narrowing of that same yellow region, indicating a less smaller extremum.

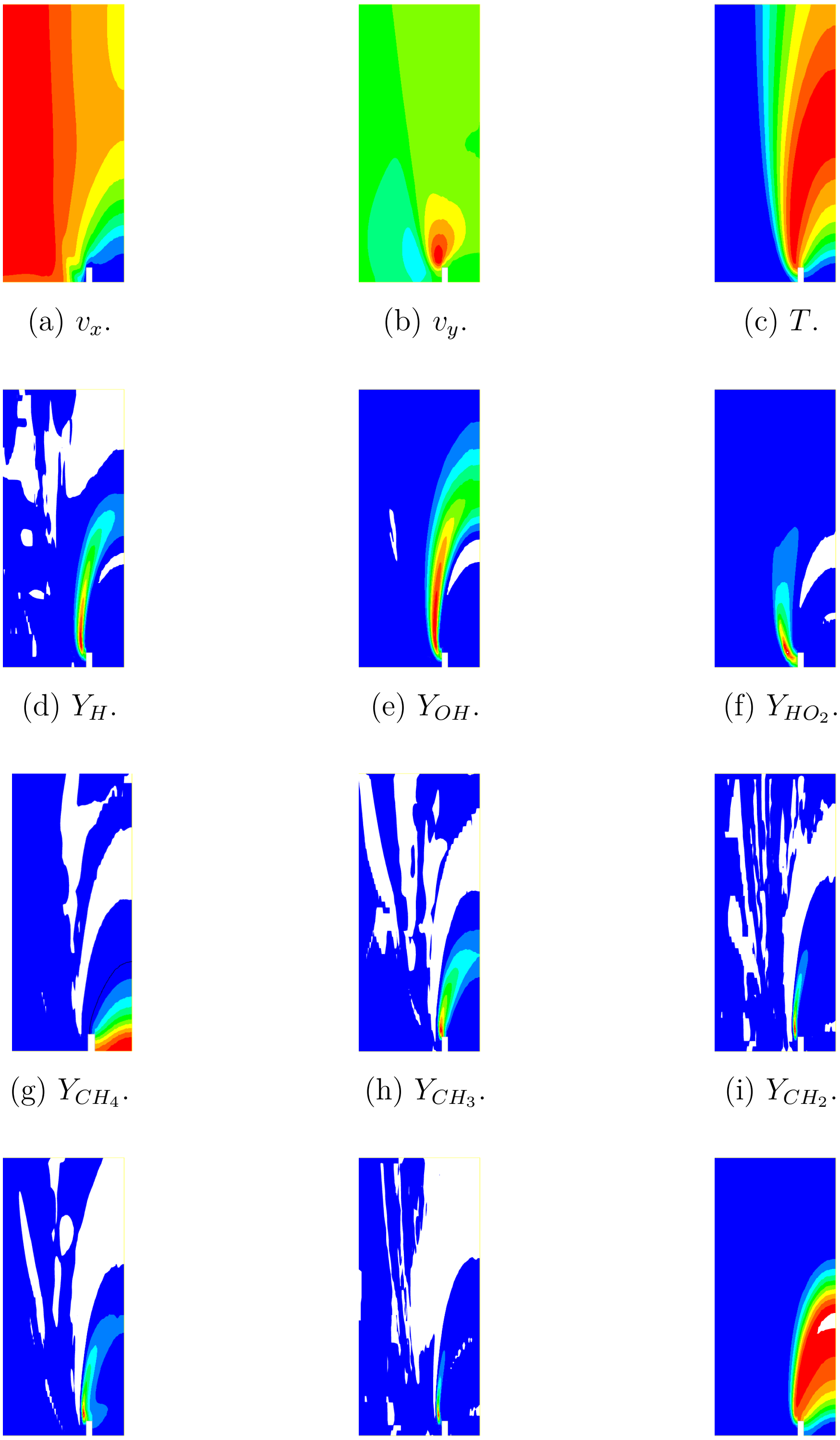

(a) v_x.

(b) v_y.

(c) T.

(d) Y_H.

(e) Y_{OH}.

(f) Y_{HO_2}.

(g) Y_{CH_4}.

(h) Y_{CH_3}.

(i) Y_{CH_2}.

(j) Y_{CH_2O}.

(k) Y_{HCO}.

(l) Y_{CO}.

Figure 3.4: Flame properties obtained with $ROM^{u|w|p}_{(12,5)}$ for the validation case with prescribed fuel inlet velocity of $v_{z|f,in} = 3.1$ cm/s. $v_x \in [0, 67.7]$ cm/s; $v_y \in [-17,\ 17]$ cm/s; $T \in [300, 2, 151]$ K. $Y_H \in [0,\ 1.1 \cdot 10^{-4}]$; $Y_{OH} \in [0,\ 3.9 \cdot 10^{-3}]$; $Y_{HO_2} \in [0,\ 2.3 \cdot 10^{-5}]$; $Y_{CH_4} \in [0,\ 1]$; $Y_{CH_3} \in [0,\ 1.2 \cdot 10^{-3}]$; $Y_{CH_2} \in [0,\ 2.8 \cdot 10^{-5}]$; $Y_{CH_2O} \in [0,\ 1.13 \cdot 10^{-4}]$; $Y_{HCO} \in [0,\ 5.1 \cdot 10^{-6}]$; $Y_{CO} \in [0,\ 5.1 \cdot 10^{-2}]$. The color map goes from blue (minimum) to red (maximum). The fuel inlet is located at the bottom right side, and at the left side is the air inlet.

The radial velocity, on the other hand, Fig. 3.4b, shows no apparent discrepancy from the CFD case. Most of the domain has zero velocity, represented by the green color, with two non-zero regions, at the fuel and air inlets vicinity, near the wall, and at the fuel tube outlet, where there is a positive and a negative region. Regarding the limits (extrema) of axial and radial velocities, this uncoupled ROM predicts the same values as those obtained by CFD. The temperature profile is shown in Fig. 3.4c, and is also quite similar to the one obtained by CFD, Fig. 3.2c. One small difference is that $ROM_{(12.5)}^{(u|w|T)}$ predicted a maximum temperature of 2,418 K, whereas the CFD-resolved maximum temperature is 2,151 K.

Examining now the chemical species, it can be seen that all reconstructed results, with notable exception CO, Figs. 3.4d - 3.4k, exhibit a negative mass fraction region, that is represented by the white color, which is physically impossible. This negative mass fraction problem in the uncoupled ROM reconstruction is found for 15 out of 20 of the reconstructed species, with various orders of magnitude. One may note that the results for OH and HO_2, Figs. 3.4e and 3.4f, show a smaller region of negative mass fraction than the others species, such as CH_2 (Fig. 3.4i). The fact that the ROM predicts a result that is not found in any CFD case suggests that the interpolation used in the ROM methodology, GARS, does not preserve neither the monotonicity nor the boundedness of the properties, which are indispensable qualities for combustion studies.

Despite these shortcomings, the species fields obtained by the uncoupled ROM are some what similar to those obtained by CFD. One notable difference is in the mass fraction of H, Fig. 3.4d, where although the $ROM_{(12.5)}^{(u|w|H)}$ reaches a maximum at symmetry axis, as in the CFD, the mass fraction of H of the uncoupled ROM is smaller than $2.2 \cdot 10^{-5}$, which is the average mass fraction concentration seen at the same region in the CFD case. Another example is the $ROM_{(12.5)}^{(u|w|CH_2)}$, Fig. 3.4i, where the characteristic length of the CH_2 field is shorter, by almost 2 mm than, that shown in Fig. 3.2i.

Finally, concerning the carbon monoxide mass fraction field of the uncoupled ROM, presented in Fig. 3.4l, one may note that the reconstructed field is slightly longer than the one given by CFD (Fig. 3.2l). Another relevant issue is that the $ROM_{(12.5)}^{(u|w|CO)}$ result shows a region with maximum mass fraction of 0.053, which is higher than the one solved by CFD, 0.051.

3.2.2
Coupled properties

The analysis of the impact of the decomposition of the data, discussed in the previous section, establish that some properties have a steeper energy decay with the number of modes than others. In addition, some chemical species exhibit a negative mass fraction region or a region where the mass fraction exceeds the expected and solved by CFD. In other words, the ROM do not respect the positivity, monotonicity and boundedness properties of the scalars. Therefore, in order to evaluate the effect of the different coupling methodologies, the comparison of the energy related to the reduced order model with the properties treated as uncoupled $\left(ROM_{(12,5)}^{(u|w|p)}\right)$ and treated as coupled $\left(ROM_{(12,5)}^{(c|w/n|all)}\right)$, is given in Fig. 3.5. This figure shows the results corresponding to three methodologies of the coupled properties, one without normalization (w), the other two cases with normalization being applied, using Eq. (2-16): one having only the temperature and velocity normalized $(n_{t,v})$, and another with all properties normalized (n_{all}).

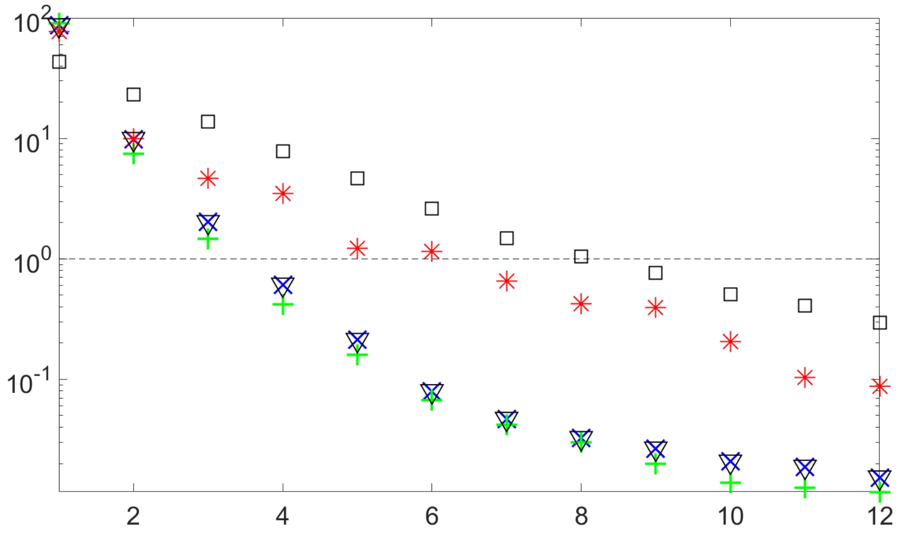

Figure 3.5: Singular values, normalized by the sum, as a function of the number of modes. The y axis is represented in a logarithm with base 10 scale and the x axis is a linear scale. $\times$: $ROM_{(12,5)}^{(c|w|all)}$; $+$: $ROM_{(12,5)}^{(c|n_{t,v}|all)}$; $*$: $ROM_{(12,5)}^{(c|n_{all}|all)}$; ∇: $ROM_{(12,5)}^{u|w|T}$; $\square$: $ROM_{(12,5)}^{u|w|OH}$.

Figure 3.5 shows that the energy required to reconstruct the ROM using the coupled properties without a normalization is similar to the energy necessary to the temperature ROM. This can be explained by considering that the singular values are controlled by the highest absolute value property, in this case temperature, which is of the order of 10^3. Despite the normalization of the temperature and velocity, the energy content is still similar to that required to reconstruct the temperature, which can be explained by the remarkable difference between the orders of magnitude of the different species, which are significantly smaller than one. In contrast, considering the coupled case with all properties normalized, one notices that the decrease of the energy present in each mode is more similar to the uncoupled OH ROM, i.e., it is slower than the other coupled ROM. One way to illustrate this is to draw a horizontal line at $y = 1$. Indeed, one notices that for both $ROM^{(c|w|all)}_{(12,5)}$ and $ROM^{(c|n_{t,v}|all)}_{(12,5)}$, in the fourth mode the energy is smaller than 1. On the other hand, for the $ROM^{(c|n_{all}|all)}_{(12,5)}$, this occurs only in the seventh mode. Therefore, these results indicate that the coupled normalized properties learning process is limited by the combustion scalars, that are “harder” to learn, which are the intermediate species.

Figure 3.6 presents the fields of the 12 flame properties for the coupled ROM without normalization. When comparing qualitatively with the $ROM^{(u|w|v_x)}_{(12,5)}$, Fig. 3.4a, it can be seen that the axial velocity profile, Fig. 3.6a, resembles the profile solved by CFD (Fig. 3.2a), having a continuous uniform velocity represented by the yellow color near the axis of symmetry, presenting only a smaller narrowness than that observed in Fig. 3.2a. Regarding the radial velocity component and the temperature profile, in a qualitatively comparison, these do not show significant differences between these two ROM results. An interesting point is that, in both reduced order models, the maximum temperature prediction is smaller than that solved by CFD (2,151 K), but are identical for the $ROM^{(u|w|T)}_{(12,5)}$ and for the $ROM^{(c|w|all)}_{(12,5)}$, the maximum temperature is 2,148 K.

Regarding the chemical species, the $ROM^{(c|w|all)}_{(12,5)}$ result also shows, for all chemical species, except CO, regions of negative mass fractions. However, a noticeable decrease of the associated white area may be seen in the fields of the H, HO_2, CH_4, CH_3, CH_2, CH_2O and HCO given in Figs. 3.6d, 3.6f, 3.6g, 3.6h, 3.6i, 3.6j, and 3.6k, respectively. For CO, Fig. 3.6l, a region is also found where the mass fraction exceeds that solved by CFD, having the same maximum mass fraction of 0.053. It is worth noting that in both, $ROM^{(u|w|p)}_{(12,5)}$ and $ROM^{(c|w|all)}_{(12,5)}$, the maximum limits of the mass fractions are the same, exhibiting only an minor discrepancy at the fifth decimal for the species: H, CH_2O, CH_3O, C_2H_5.

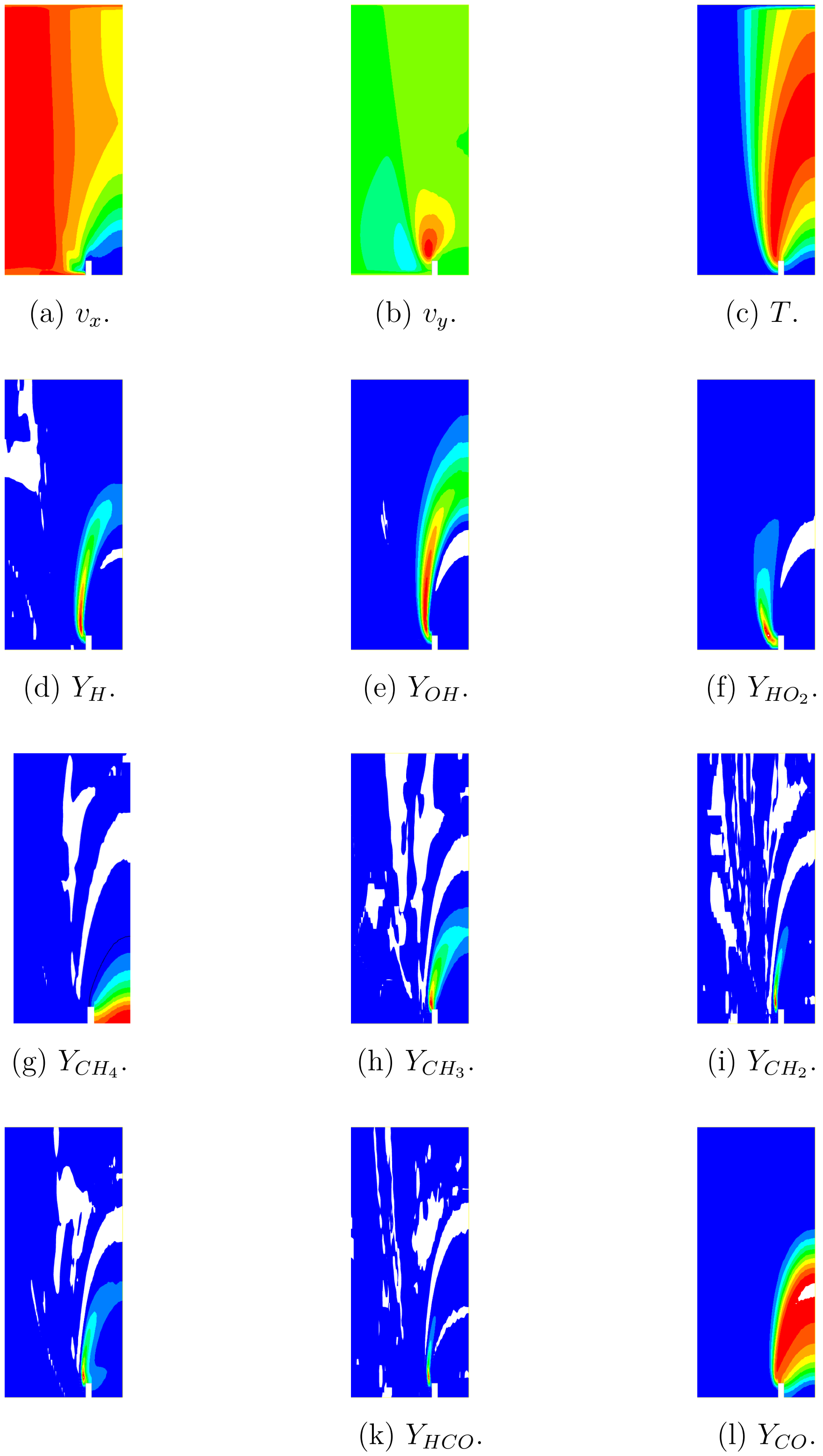

(a) v_x.

(b) v_y.

(c) T.

(d) Y_H.

(e) Y_{OH}.

(f) Y_{HO_2}.

(g) Y_{CH_4}.

(h) Y_{CH_3}.

(i) Y_{CH_2}.

(k) Y_{HCO}.

(l) Y_{CO}.

Figure 3.6: Flame properties obtained with $ROM_{(12,5)}^{(c|w|all,p)}$ for the validation case with prescribed fuel inlet velocity of $v_{z|f,in} = 3.1$ cm/s. The color map limits are $v_x \in [0, 67.7]$ cm/s; $v_y \in [-17,\ 17]$ cm/s; $T \in [300, 2, 151]$ K. $Y_H \in [0,\ 1.1 \cdot 10^{-4}]$; $Y_{OH} \in [0,\ 3.9 \cdot 10^{-3}]$; $Y_{HO_2} \in [0,\ 2.3 \cdot 10^{-5}]$; $Y_{CH_4} \in [0,\ 1]$; $Y_{CH_3} \in [0,\ 1.2 \cdot 10^{-3}]$; $Y_{CH_2} \in [0,\ 2.8 \cdot 10^{-5}]$; $Y_{CH_2O} \in [0,\ 1.13 \cdot 10^{-4}]$; $Y_{HCO} \in [0,\ 5.1 \cdot 10^{-6}]$; $Y_{CO} \in [0,\ 5.1 \cdot 10^{-2}]$. The color map goes from blue (minimum) to red (maximum). The fuel inlet is located at the bottom right side, and at the left side is the air inlet.

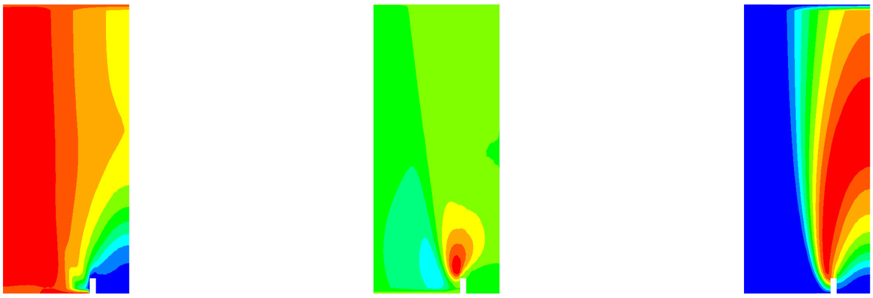

(a) v_x. (b) v_y. (c) T.

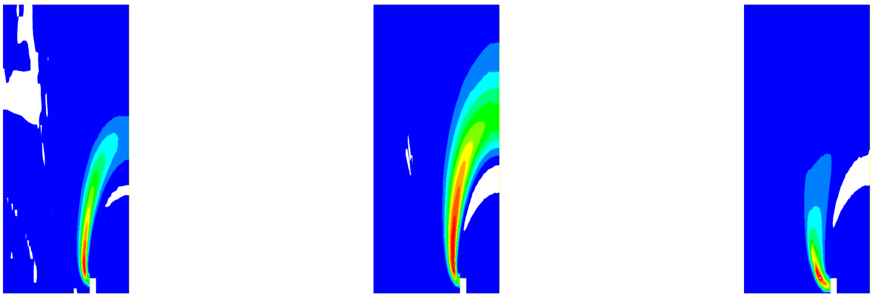

(d) Y_H. (e) Y_{OH}. (f) Y_{HO_2}.

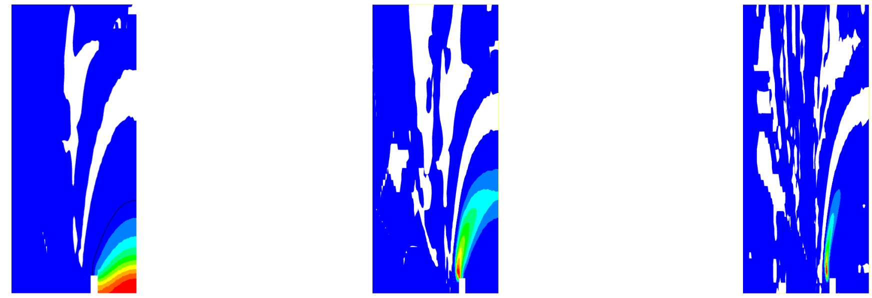

(g) Y_{CH_4}. (h) Y_{CH_3}. (i) Y_{CH_2}.

(j) Y_{CH_2O}. (k) Y_{HCO}. (l) Y_{CO}.

Figure 3.7: Flame properties obtained with $ROM_{(12,5)}^{(c|n_{t,v}|all,p)}$ for the validation case with prescribed fuel inlet velocity of $v_{z|f,in} = 3.1$ cm/s. The color map limits are $v_x \in [0, 67.7]$ cm/s; $v_y \in [-17,\ 17]$ cm/s; $T \in [300, 2, 151]$ K. $Y_H \in [0,\ 1.1 \cdot 10^{-4}]$; $Y_{OH} \in [0,\ 3.9 \cdot 10^{-3}]$; $Y_{HO_2} \in [0,\ 2.3 \cdot 10^{-5}]$; $Y_{CH_4} \in [0,\ 1]$; $Y_{CH_3} \in [0,\ 1.2 \cdot 10^{-3}]$; $Y_{CH_2} \in [0,\ 2.8 \cdot 10^{-5}]$; $Y_{CH_2O} \in [0,\ 1.13 \cdot 10^{-4}]$; $Y_{HCO} \in [0,\ 5.1 \cdot 10^{-6}]$; $Y_{CO} \in [0,\ 5.1 \cdot 10^{-2}]$. The color map goes from blue (minimum) to red (maximum). The fuel inlet is located at the bottom right side, and at the left side is the air inlet.

The results of the ROM using the coupled methodology with temperature and velocity normalization, shown in Fig. 3.7, are quite similar to those obtained by the coupled ROM without normalization (Fig. 3.6). For this reason only a brief analysis of these data is performed.

In a qualitative comparison, the chemical species fields of the $ROM^{(c|n_{t,v}|all)}_{(12,5)}$ resemble those of the $ROM^{(c|w|all)}_{(12,5)}$ and $ROM^{(u|w|all)}_{(12,5)}$, when comparing the overall structure, thickness, and characteristic length of the 9 chosen species. Despite the normalization of temperature and velocity, there is no perceivable decrease in the negative mass fraction regions, or a significant change from the mass fraction extrema. The maximum temperature in the coupled ROM with the temperature and velocity normalization is 2,418 K also. It is interesting to note that in the SVD modes energy distribution, shown in Fig. 3.5, the $ROM^{(c|n_{t,v}|all)}_{(12,5)}$ is quite similar to the $ROM^{(c|w|all)}_{(12,5)}$, which underscores the observed fields similarity of the reconstructed properties.

However, the results obtained with the coupled ROM using the data from all species normalized, Fig. 3.8, are different to those from the other coupled ROM. For the velocity components, Figs. 3.8a and 3.8b show fields quite similar to those obtained by CFD. The temperature field, Fig. 3.8c, is also quite similar, qualitatively speaking, to those obtained by the other ROM. However, the maximum temperature seen in the $ROM^{(c|n_{all}|all)}_{(12,5)}$ is 2,120 K, which is smaller than the ones obtained in the other two coupled ROM and in the uncoupled ROM.

Regarding the chemical species, Figs 3.8d - 3.8l, one may notice that the negative mass fraction region is decreased when compared to the other reduced order model results (Figs. 3.4, 3.6 and 3.7). Yet 10 species still exhibit regions of negative mass fraction, in particular: H, O, OH, CH_3, CH_2, and HCO. Nevertheless, the order of magnitude of these negative regions has been reduced, going from 10^{-3} to 10^{-8}.

A major difference between the results obtained by the reduced order model methodology, for $ROM^{(c|n_{all}|all)}_{(12,5)}$, is seen in the fields of the chemical species: H, OH, CH_3, CH_2, CH_2O and HCO (Figs. 3.8d, 3.8e, 3.8h, 3.8i, 3.8j and 3.8k). Indeed, that these fields exhibit a spatial bifurcation. In addition, the CH_3 profile is more spread out and less defined when compared to the other results (Figs. 3.4h, 3.6h and 3.7h). This problem could perhaps be overcomed by adding new cases to the dataset given in the learning step [82].

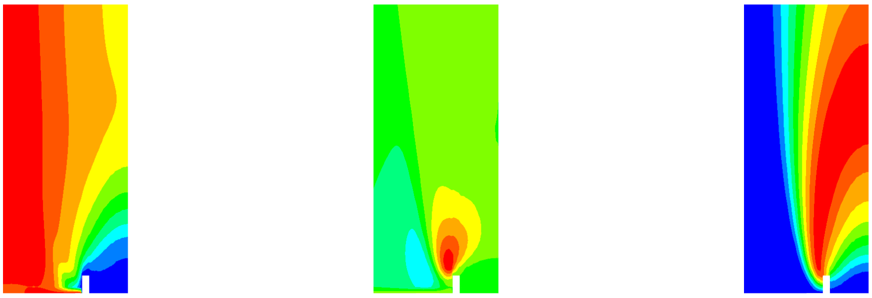

(a) v_x. (b) v_y. (c) T.

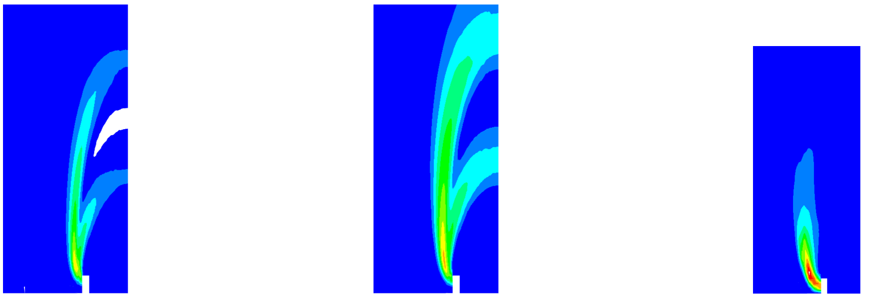

(d) Y_H. (e) Y_{OH}. (f) Y_{HO_2}.

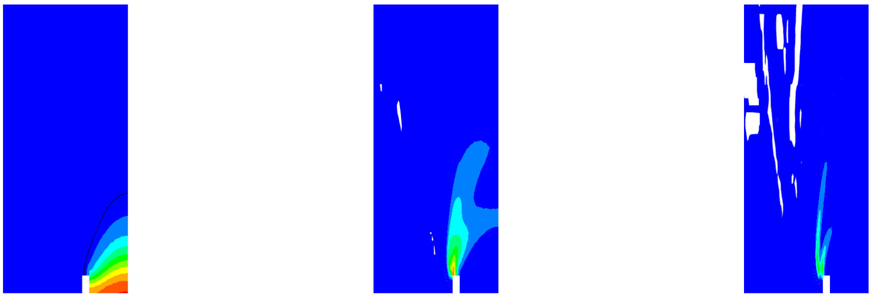

(g) Y_{CH_4}. (h) Y_{CH_3}. (i) Y_{CH_2}.

(j) Y_{CH_2O}. (k) Y_{HCO}. (l) Y_{CO}.

Figure 3.8: Flame properties obtained with $ROM_{(12,5)}^{(c|n_{all}|all,p)}$ for the validation case with prescribed fuel inlet velocity of $v_{z|f,in} = 3.1$ cm/s. The color map limits are $v_x \in [0, 67.7]$ cm/s; $v_y \in [-17,\ 17]$ cm/s; $T \in [300, 2, 151]$ K. $Y_H \in [0,\ 1.1 \cdot 10^{-4}]$; $Y_{OH} \in [0,\ 3.9 \cdot 10^{-3}]$; $Y_{HO_2} \in [0,\ 2.3 \cdot 10^{-5}]$; $Y_{CH_4} \in [0,\ 1]$; $Y_{CH_3} \in [0,\ 1.2 \cdot 10^{-3}]$; $Y_{CH_2} \in [0,\ 2.8 \cdot 10^{-5}]$; $Y_{CH_2O} \in [0,\ 1.13 \cdot 10^{-4}]$; $Y_{HCO} \in [0,\ 5.1 \cdot 10^{-6}]$; $Y_{CO} \in [0,\ 5.1 \cdot 10^{-2}]$. The color map goes from blue (minimum) to red (maximum). The fuel inlet is located at the bottom right side, and at the left side is the air inlet.

Figure 3.8g shows the CH_4 mass fraction, one may see that the fuel concentration inside the tube, near the fuel outlet (bottom right corner) is less than 1, more precisely, around 0.8. The methane concentration starts to decrease at $x = 57\ mm$, 3 mm before the fuel feeding tube outlet. In contrast, the CO mass fraction of $ROM^{(c|n_{all}|all)}_{(12,5)}$ (Fig. 3.8l) has a region of maximum concentration, around 2.5 mm, which is smaller than that of $ROM^{(u|w|CO)}_{(12,5)}$, $ROM^{(c|w|all)}_{(12,5)}$ and $ROM^{(c|n_{t,v}|all)}_{(12,5)}$. In addition, the mass fraction of CO is more spread out along the x direction, and for the $ROM^{(c|n_{all}|all)}_{(12,5)}$ the maximum CO height is 34 mm, from the outlet of the fuel feeding tube.

In order to further characterize the apparent minor species fields bifurcations, a number of learning modes and cases is now increased. For that matter, three new reduced order models are constructed. Two using 12 learning cases with 10 and 12 modes, and one using 16 learning cases (80% of the dataset cases) and 10 modes. These showed that, despite the increase in the number of modes and learning cases, the problem in describing the species remains a difficult task, and significant differences have not been obtained. On a positive note, the negative mass fraction region slightly decreased. Since no remarkable differences were obtained, and for the sake of brevity, such results are not presented here.

One of the major concerns regarding the numerical simulations involving combustion is mass conservation, which is commonly expressed as $\sum Y_i = 1$. Thus, to verify that the ROM methodology does guarantee mass conservation, an analysis of the residual of this sum, i.e., $r_{Y_i} = 1 - \sum Y_i$ was performed also. It is worth noticing that, although some of the chemical species reconstructions present negative mass fractions regions, in none of the ROM the conservation of mass is violated. Indeed, the reconstructed r_{Y_i} error is randomly distributed for all ROM, having a maximum standard deviation of continuity of 10^{-7}. These results are not given here for the sake of brevity.

3.2.3
Logarithm of species pre-processing

Aiming to solve the monotonicity problem faced by the uncoupled and coupled ROM, here the application of the logarithm to the learning data is proposed, as given by Eqs. (2-17) - (2-18). In order to study the influence of this method, the effect of truncation parameter is first analyzed, for three values of ϵ_c, where ϵ_c is the negative exponent of the truncation parameter. The values of ϵ_c arbitrarily chosen are 8, 10 and 12.

Accordingly, three reduced order models, using the logarithm technique presented in section 2.3.1, are constructed for those values of ϵ_c. Figure 3.9

presents the corresponding singular values normalized by the sum, as a function of the number of modes for four species, one minor (CH_2), one intermediate (OH) and two major species (CO and CO_2).

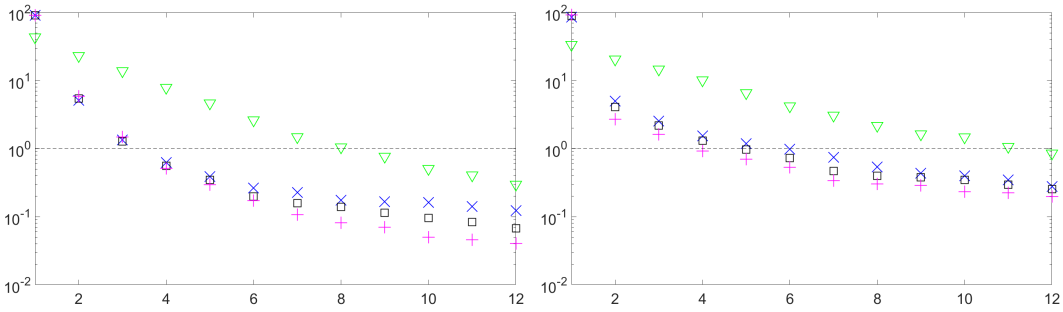

(a) Y_{OH} (b) Y_{CH_2}

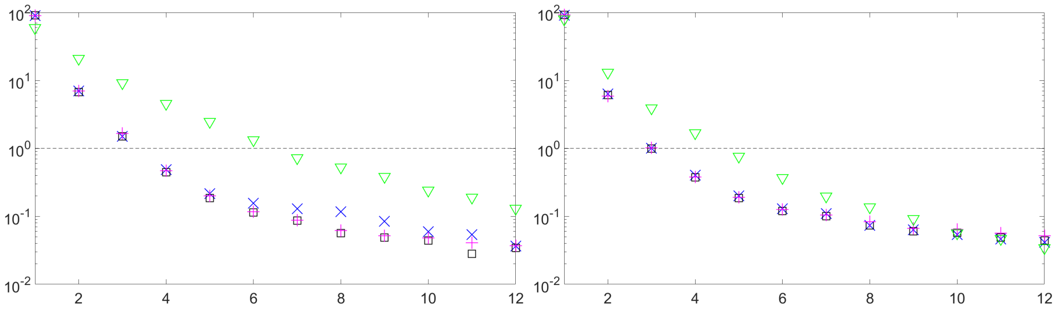

(c) Y_{CO} (d) Y_{CO_2}

Figure 3.9: Singular values normalized by the sum as a function of the number of modes for the $ROM_{(12,5)}^{(u|w|p)}$ and $ROM_{(12,5)}^{(u|l|p)}$, for three different truncation parameters. ϵ_c is the negative exponent of the truncation parameter chosen as the minimum value of the mass fraction range. $\bigtriangledown$: $ROM_{(12,5)}^{(u|w|p)}$; $+$: $\epsilon_c = 8$; $\square$: $\epsilon_c = 10$; $\times$: $\epsilon_c = 12$. The y axis is represented in a logarithm with base 10 scale and the x axis is a linear scale.

A qualitatively similar behavior is noticed for all results shown in Fig. 3.9. Indeed, the singular values of $ROM_{(12,5)}^{(u|w|p)}$ are larger than those found for $ROM_{(12,5)}^{(u|l|p)}$, for every mode. Also, for all species, except CO_2, the singular values of the uncoupled ROM are at least an order of magnitude larger than for the ROM where the logarithm pre-processing is applied to the learning data.

Regarding the singular values corresponding to the different truncation parameters, for the mass fraction of OH, seen in Fig. 3.9a, initially there is no significant discrepancy. However, beyond the sixth mode, a difference between the singular values for each one of the truncation parameters ϵ_c is observed. For instance, for the parameter, $\epsilon_c = 12$, the mode values are larger than when $\epsilon_c = 8$. Regarding the minor species CH_2, given in Fig. 3.9b, one may notice a difference between the singular values, starting from the second mode. Also, when $\epsilon_c = 12$, the decrease is smaller when compared to $\epsilon_c = 10$ and 8. For the major species CO and CO_2, Fig. 3.9c and Fig. 3.9d, the singular values corresponding to the three ϵ_c chosen are remarkably similar.

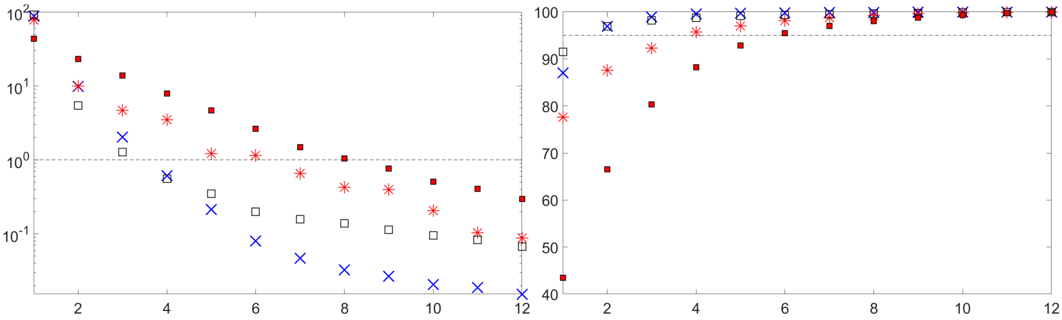

(a) (b)

Figure 3.10: Singular values normalized by sum (a) and the cumulative energy (b) as a function of the number of modes. ■: $ROM^{(u|w|OH)}_{(12,5)}$; □: $ROM^{(u|l|OH)}_{(12,5)}$; ×: $ROM^{(c|w|all)}_{(12,5)}$; ∗: $ROM^{(c|n_{all}|all)}_{(12,5)}$.

The energy of the SVD modes can be represented in at least two forms, the first one as the energy present in each mode, and the other as the cumulative sum of this energy, as given in Fig. 3.10. As previously stated, as the number of modes increases the energy of each mode decreases, and consequently the cumulative energy increases. Figure 3.10 displays both the singular values normalized by the sum (Fig. 3.10a) and the cumulative energy (Fig. 3.10b) for the $ROM^{(u|w|OH)}_{(12,5)}$, $ROM^{(c|w|all)}_{(12,5)}$, $ROM^{(c|n_{all}|all)}_{(12,5)}$, and $ROM^{(u|l|OH)}_{(12,5)}$. One may notice that the singular values of the $ROM^{(u|l|OH)}_{(12,5)}$, until the fourth mode, have a similar behavior to the $ROM^{(c|w|all)}_{(12,5)}$, and from the sixth mode forward, this steepness becomes smaller. In addition, in the eleventh and twelfth modes, the energy of the $ROM^{(u|l|OH)}_{(12,5)}$ is very close to the $ROM^{(c|n_{all}|all)}_{(12,5)}$ energy.

In particular, the energy decrease is higher when the logarithm is applied to the species, when compared to the uncoupled ROM of the chemical species. An interesting point is that the energy present in the first mode is highest for the $ROM^{(u|l|OH)}_{(12,5)}$, followed by the $ROM^{(c|w|all)}_{(12,5)}$, $ROM^{(c|n_{all}|all)}_{(12,5)}$, and $ROM^{(u|w|OH)}_{(12,5)}$, this is more clearly seen in Fig. 3.10b.

In order to further analyze the influence of the ϵ_c truncation parameter on the reconstruction of the chemical species fields, Fig. 3.11 exhibits the OH mass fraction for the three ϵ_c chosen. Notably, there is no visible qualitative difference between these three fields, and they also resemble the field obtained with CFD, Fig. 3.2e. Moreover, the apparent monotonicity problem seen in the previous OH mass fraction results seems to be solved when using such logarithm pre-processing method. To further assess whether this data pre-processing indeed solves the positivity, monotonicity and boundedness mass fraction problem, Fig. 3.12 presents fields of the 9 species (H, OH, HO_2, CH_4, CH_3, CH_2, CH_2O, HCO and CO) discussed previously in this work.

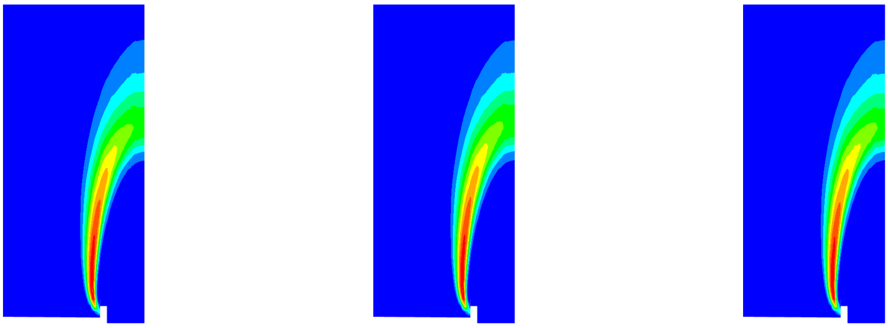

(a) $\epsilon_c = 12$. (b) $\epsilon_c = 10$. (c) $\epsilon_c = 8$.

Figure 3.11: OH mass fraction field obtained with the uncoupled reduced order model, using as learning data the logarithm of the chemical species data for three different ϵ_c, for the validation case with prescribed fuel inlet velocity of $v_{z|f,in} = 3.1$ cm/s. ϵ_c is the negative exponent of the truncation parameter chosen for the data that the logarithm is applied as the minimum value of the mass fraction range. The OH mass fraction varies between $[0,\ 3.8 \cdot 10^{-3}]$. The color map goes from blue (minimum) to red (maximum). The fuel inlet is located at the bottom right side, and at the left side is the air inlet.

The main difference observed in the $ROM^{(u|l|p)}_{(12,5)}$ results is that none of chemical species reconstructions present a negative mass fraction region. In fact, the minima of all the mass fractions obtained are positive and greater than zero, on the order of magnitude of 10^{-11}. Note that some of the fields obtained using the logarithm pre-processing methodology are somewhat similar to the other ROM. However, the results for the mass fraction of CH_3 and CH_2O, Figs. 3.12e and 3.12g, are discrepant. Indeed, one may note that the mass fraction of CH_3 maximum along the symmetry axis is clearly visible. Concerning the mass fraction of CH_2O, there is a local maximum at the symmetry axis, which is not seen in the CFD case (Fig. 3.2).

It is worth to note that Fig. 3.12d shows two horizontal colored lines at the top and bottom left of the image. This is due to the interpolation of the results in the mesh, and does not interferes with the CH_4 mass fraction field. Regarding the CO mass fraction field, Fig. 3.12i, it is noted that there is still a region with a $Y_{CO} > 0.051$, similar to that found in the $ROM^{(u|w|CO)}_{(12.5)}$, $ROM^{(c|w|all,CO)}_{(12.5)}$ and $ROM^{(c|n_{t,v}|all,CO)}_{(12.5)}$. Concerning the continuity criteria, the maximum standard deviation increases to 10^{-5}, but the error ($r_{Y_i} = 1 - \sum Y_i$) still remains randomly distributed.

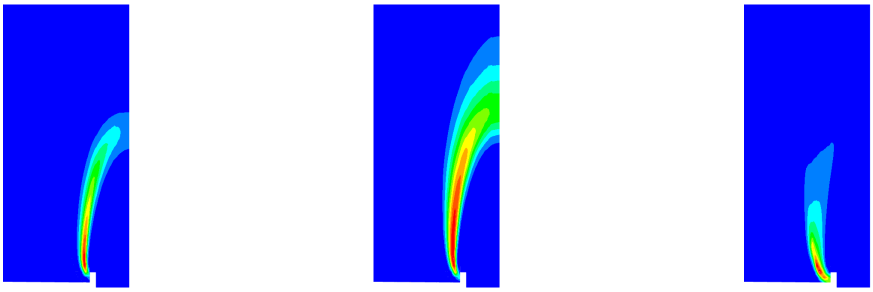

(a) Y_H. (b) Y_{OH}. (c) Y_{HO_2}.

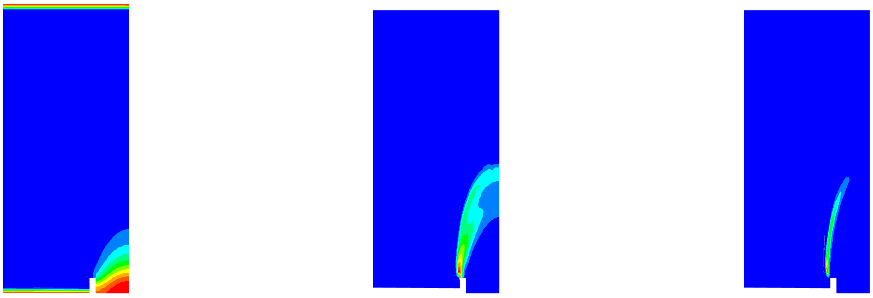

(d) Y_{CH_4}. (e) Y_{CH_3}. (f) Y_{CH_2}.

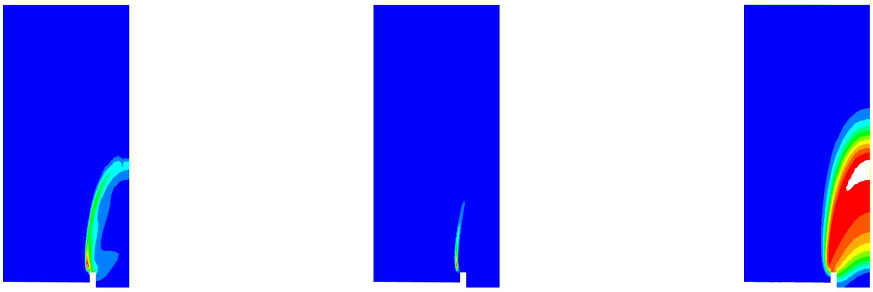

(g) Y_{CH_2O}. (h) Y_{HCO}. (i) Y_{CO}.

Figure 3.12: Flame species obtained with $ROM^{(u|l|p)}_{(12,5)}$ for $\epsilon_c = 10$, for the validation case with prescribed fuel inlet velocity of $v_{z|f,in} = 3.1$ cm/s. The color map limits are $Y_H \in [0,\ 1.1 \cdot 10^{-4}]$; $Y_{OH} \in [0,\ 3.9 \cdot 10^{-3}]$; $Y_{HO_2} \in [0,\ 2.3 \cdot 10^{-5}]$; $Y_{CH_4} \in [0,\ 1]$; $Y_{CH_3} \in [0,\ 1.2 \cdot 10^{-3}]$; $Y_{CH_2} \in [0,\ 2.8 \cdot 10^{-5}]$; $Y_{CH_2O} \in [0,\ 1.13 \cdot 10^{-4}]$; $Y_{HCO} \in [0,\ 5.1 \cdot 10^{-6}]$; $Y_{CO} \in [0,\ 5.1 \cdot 10^{-2}]$. The color map goes from blue (minimum) to red (maximum). The fuel inlet is located at the bottom right side, and at the left side is the air inlet.

As a further analysis of the effect of this pre-processing step, Figs. 3.13 and 3.14 shows along the symmetry axis the mass fractions of OH and CO, respectively. Figure 3.13a shows the mass fraction of OH along the axis of symmetry for the CFD results, $ROM^{(u|w|OH)}_{(12.5)}$ and $ROM^{(u|l|OH)}_{(12.5)}$. Analyzing these results one may confirm that the curve corresponding to $ROM^{(u|w|OH)}_{(12,5)}$ exhibits a non-monotonic behavior between 70 and 80 mm, i.e., the OH mass fraction increases and then decreases to a negative value, which is physically impossible, returning to a positive value near 80 mm. Regarding the $ROM^{(u|l|OH)}_{(12.5)}$ results, Fig. 3.13a shows that a distinction between the different curves (different ϵ_c values) and the CFD result is not observed until 80 mm. The CFD result has a maximum OH mass fraction slightly upstream, when compared to the other curves. As for the maximum OH mass fraction, the curves of CFD and $\epsilon_c = 8$ are the largest, and the peak of the curve of $ROM^{(u|w|OH)}_{(12.5)}$ is the smallest. Nevertheless, the curves of $ROM^{(u|l|OH)}_{(12.5)}$ for $\epsilon_c = 10$ and 12 are quite similar to each other.

Examining now the logarithm representation of the OH mass fraction, given at Fig. 3.13b, one can further verify the influence of the chosen truncation value. As expected, truncating $\epsilon_c = 8$ loses the most information, i.e., nearly all the information between the 60 and 65 mm. However, for $\epsilon_c = 12$, the curve closely resembles the CFD curve, and for $\epsilon_c = 10$, the curve loses a smaller amount of information than for $\epsilon_c = 8$ in the same interval. Downstream 65 mm, no significant difference between the CFD results and the different $ROM^{(u|l|OH)}_{(12.5)}$ is seen. Furthermore, this logarithm representation shows that, regarding $ROM^{(u|w|OH)}_{(12.5)}$, an Y_{OH} increase occurs upstream the other results and, they only agree downstream 80 mm. Moreover, between 70 and 75 mm an oscillation is seen in the curve, where the non-monotonic behavior in Fig. 3.13a is seen. Moreover, one may note that in the logarithm of OH mass fraction curve of the uncoupled ROM, there is a segment without the dashed line, between 75 - 80 mm, since this is the location where the OH mass fraction is negative in Fig. 3.13a

Figures 3.14a and 3.14b depict the results corresponding to the carbon monoxide mass fraction and its logarithm representation, respectively. These figures show rather minor quantitative discrepancies between the ROM and CFD results. One difference from the CO mass fraction is near the 70 mm region. Indeed, in Fig. 3.14a, the CFD and $\epsilon_c = 12$ curves continue to rise until reaching a maximum, near 75 mm. Discrepancy from the other curves, which show a slower increase until at this position, where it starts to rise more rapidly, before reaching a maximum near 75 mm.

The obtained results clearly underscore the benefits of using the logarithm pre-processing of the data prior the learning step. Indeed, both the monotonicity and boundedness properties are preserved, and learning is achieved with a smaller number of modes, when compared to the unprocessed data. The success of this strategy may be attributed to the fact that the exponential tails of the chemical species spatial distribution, which contain relevant data to be learned, and are thus better captured. Furthermore, this pre-processing step effectively spatially widens the fields of minor species, which also eases the learning. Finally, this pre-processing also should provide a more generalizable re-scaling of species mass fractions and other properties that span over several orders of magnitude.

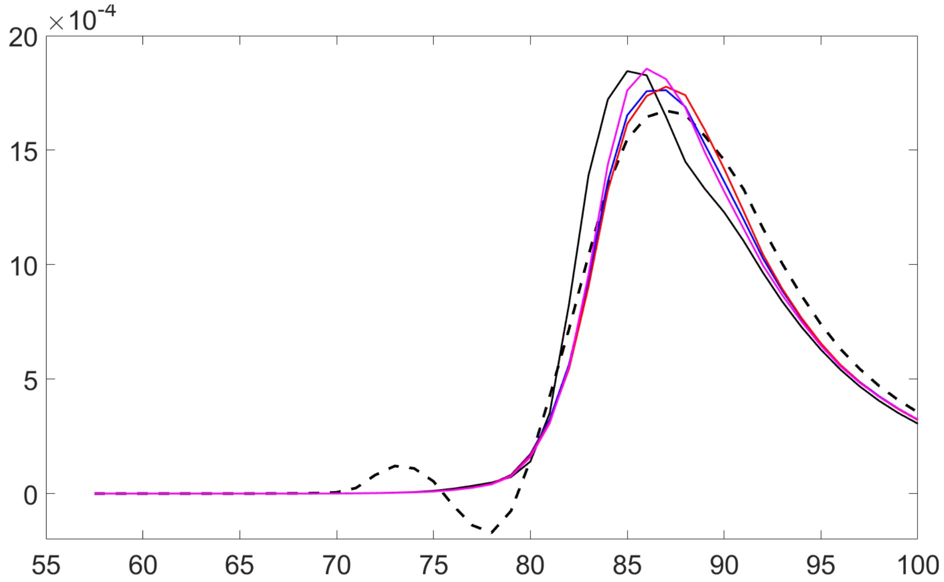

(a) Y_{OH}.

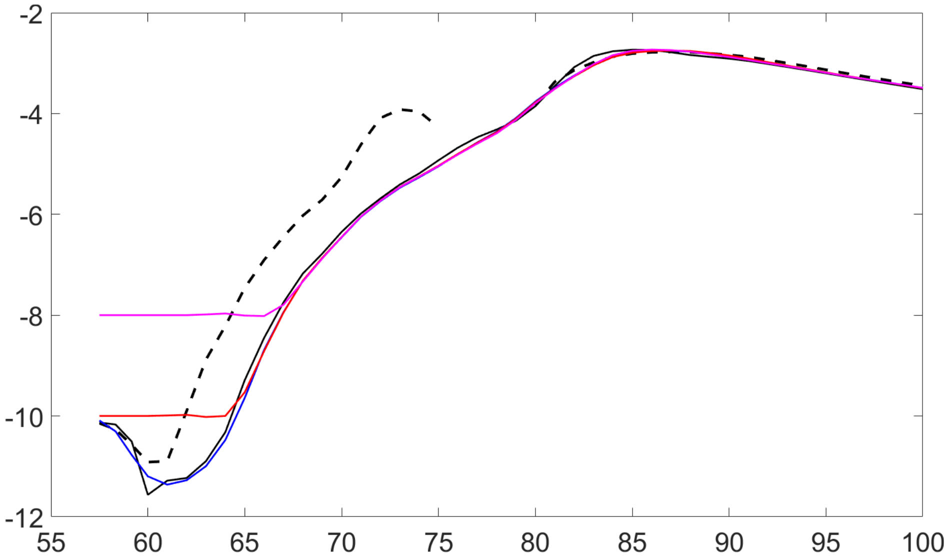

(b) $\log_{10} Y_{OH}$.

Figure 3.13: Mass fractions of OH along the symmetry axis. The y axis is the species mass fraction and the x axis is the distance in the flow direction [mm], where 60 mm is the outlet of the fuel's feeding tube. Black solid line: CFD; black dashed line: $ROM_{(12,5)}^{(u|w|OH)}$; colored lines: $ROM_{(12,5)}^{(u|l|OH)}$, where the different colors represents each truncation parameter (ϵ_c) analyzed. $\epsilon_c = 8$ is represented by the magenta line, $\epsilon_c = 10$ by the red line, and $\epsilon_c = 12$ by the blue line.

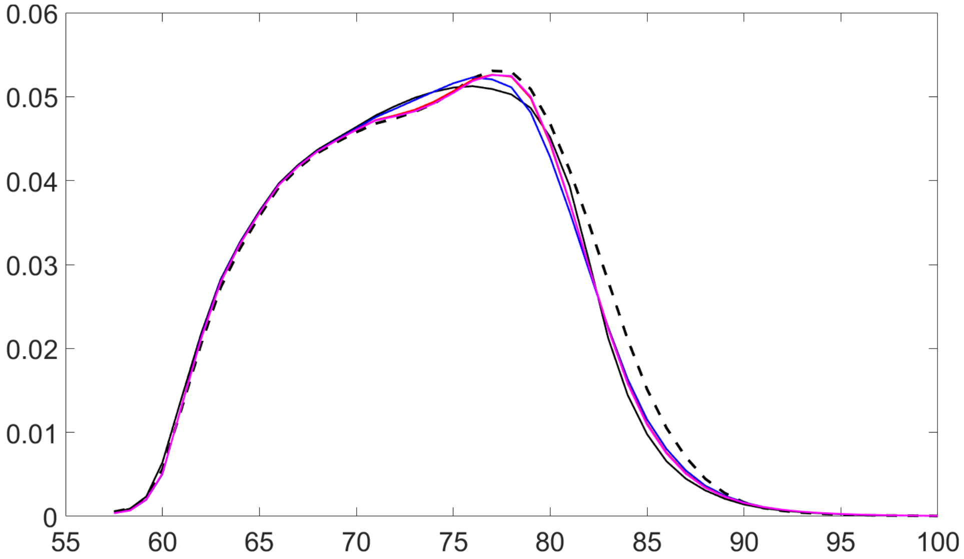

(a) Y_{CO}.

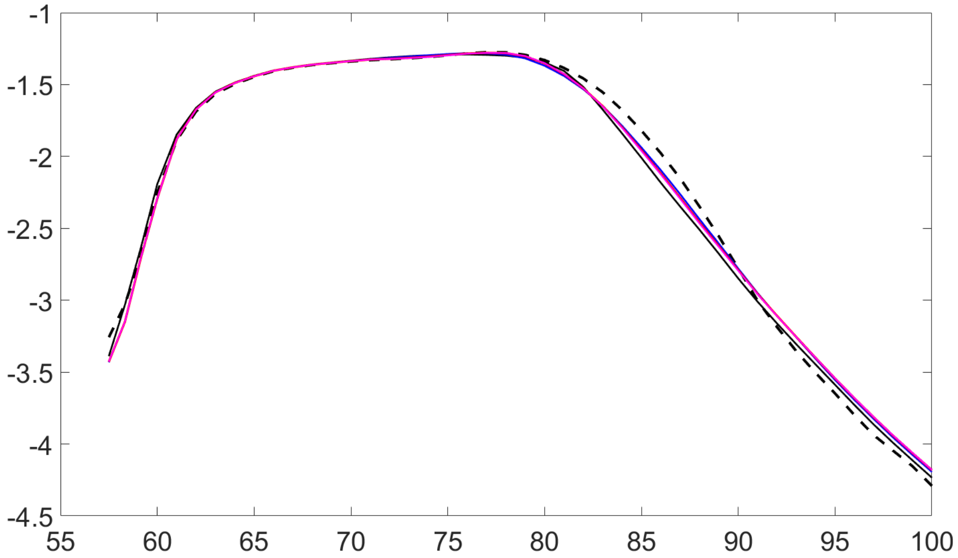

(b) $\log_{10} Y_{CO}$.

Figure 3.14: Mass fractions of CO along the symmetry axis. The y axis is the species mass fraction and the x axis is the distance in the flow direction [mm], where 60 mm is the outlet of the fuel's feeding tube. Black solid line: CFD; black dashed line: $ROM^{(u|w|CO)}_{(12,5)}$; colored lines: $ROM^{(u|l|CO)}_{(12,5)}$, where the different colors represents each truncation parameter (ϵ_c) analyzed. $\epsilon_c = 8$ is represented by the magenta line, $\epsilon_c = 10$ by the red line, and $\epsilon_c = 12$ by the blue line.

4
Conclusion and perspectives

In this work, a study of different reduced order models of an non-premixed laminar flame has been performed using the data from computational fluid dynamics simulations to learn these models. This study aimed to compare the impact of different data pre-processing methodologies on the data reduction and reconstruction of the flame property fields. Besides the qualitative and quantitative comparison between CFD and ROM results, an energy analysis as a function of the modes of the singular value decomposition algorithm, has been performed for each constructed ROM.

The reduced order model was built from the fields of 23 flame properties obtained by CFD, where only the fuel inlet velocity varies. In order to reduce the computational cost of reactive simulations associated with the mesh and the number of chemical reactions to be solved, an adaptive mesh tool based on the temperature gradient and a reduced chemical kinetics mechanism were used. Despite this, each CFD simulation has required, an average of 15 days to reach convergence. Usually, machine learning algorithms require a large amount of data. Yet, despite this, the database to construct the ROM was created from 20 CFD simulations of different fuel inlet velocities.

A total of five approaches to data pre-processing have been adopted. The first one is the decoupled ROM, where each property has its own ROM. Then, it has been proposed to treat the properties as a single system, since in combustion the properties are coupled. Thus, three coupled ROM have been created, one without normalization of the properties, another with temperature and velocity normalization, and a third with all properties normalized. All these ROM presented a problem in the reconstructed fields: the presence of negative mass fraction regions. In other words, the machine learning algorithm does not guarantee the monotonicity, positivity, and boundedness of the properties, and these are important in combustion scalars. Furthermore, the reconstruction of the coupled ROM with all the properties normalized shows bifurcations in some fields, such as OH mass fraction, which suggested that the number of data provided for the ROM is insufficient.

The last pre-processing approach studied is the proposed logarithm of the chemical species. The original obtained results show that monotonicity and boundedness problems are overcome. Furthermore, when compared to the uncoupled chemical species ROM, the learning is achieved with a smaller number of modes. In light of the obtained results, perspectives for this work include:

- Increase the dataset of CFD simulations, since the accuracy of the reduced model is related to the amount of data provided in the learning step [25, 82]. In particular, the influence of the number of learning cases should be assessed, for the case of the coupled ROM with all normalized properties.
- The analysis of the influence of flame properties coupling using the logarithm of the chemical species. This would provide two relevant information on the system under study: the properties couplings and the exponential tails of the chemical species spatial distribution.
- The development of monotonicity preserving high-order interpolation method, e.g., essentially non-oscillatory (ENO) or weighted ENO (WENO) on the ROM result. These methods have been applied to problems such as aero-acoustics and image processing and would need to be extended to the present context.
- Application of ROM methodology to a three-dimensional flame configuration case using, for instance, a square cross-section burner. This three-dimensional simulation, which should increase the complexity of the problem has been initiated, but limitations on the computer availability due to multiple and frequent power outages have precluded its conclusions.

Bibliography

[1] ZHAO, F.; YANG, W. ; YU, W.. **A progress review of practical soot modelling development in diesel engine combustion**. Journal of Traffic and Transportation Engineering (English Edition), 7(3):269–281, 2020. Special Issue: Clean Alternative Fuels for Transport Vehicles.

[2] CREMER, M.; ADAMS, B.; VALENTINE, J.; LETCAVITS, J. J. ; VIERSTRA, S.. **Use of CFD modeling to guide design and implementation of overfire air for nox control in coal-fired boilers**. In: 19TH ANNUAL INTERNATIONAL PITTSBURGH COAL CONFERENCE, Pittsburgh, USA, 2002.

[3] TUTTLE, J. F.; BLACKBURN, L. D. ; POWELL, K. M.. **On-line classification of coal combustion quality using nonlinear SVM for improved neural network NOx emission rate prediction**. Computers & Chemical Engineering, 141:106990, 2020.

[4] LAW, C. K.. **Combustion physics**. Cambridge University Press, jan 2006.

[5] VERDUGO, I.; CRUZ, J. J.; ÁLVAREZ, E.; RESZKA, P.; FIGUEIRA DA SILVA, L. F. ; FUENTES, A.. **Candle flame soot sizing by planar time-resolved laser-induced incandescence**. Scientific Reports, 10(11364), 2020.

[6] INCROPERA, F. P.; DEWITT, D. P.; BERGMAN, T. L. ; LAVINE, A. S.. **Fundamentals of heat and mass transfer**. John Wiley & Son, 6th edition, 2007.

[7] PATANKAR, S. V.. **Numerical Heat Transfer and Fluid Flow**. CRC Press, 1st edition, 1980.

[8] FRIEDRICH, R.; PEINKE, J. ; KAMPS, O.. **Fluid Dynamics: Turbulence**, p. 1–26. Springer Berlin Heidelberg, Berlin, Heidelberg, 2017.

[9] PETERS, N.. **Multiscale combustion and turbulence**. Proceedings of the Combustion Institute, 33(1):1–25, 2009.

[10] GÜLDER, Ö. L.; SNELLING, D. R.. **Influence of nitrogen dilution and flame temperature on soot formation in diffusion flames.** Combustion and Flame, 92(1):115–124, 1993.

[11] JEREZ, A.; CRUZ VILLANUEVA, J.; FIGUEIRA DA SILVA, L.; DEMARCO, R. ; FUENTES, A.. **Measurements and modeling of PAH soot precursors in coflow ethylene/air laminar diffusion flames.** Fuel, 236:452–460, 2019.

[12] LIU, F.; HUA, Y.; WU, H.; FON LEE, C. ; HE, X.. **An experimental study on soot distribution characteristics of ethanol-gasoline blends in laminar diffusion flames.** Journal of the Energy Institute, 91(6):997–1008, 2018.

[13] ESCUDERO, F.; FUENTES, A.; CONSALVI, J.-L.; LIU, F. ; DEMARCO, R.. **Unified behavior of soot production and radiative heat transfer in ethylene, propane and butane axisymmetric laminar diffusion flames at different oxygen indices.** Fuel, 183:668 – 679, 2016.

[14] LIU, Y.; CHENG, X.; QIN, L.; WANG, X.; YAO, J. ; WU, H.. **Experimental investigation on soot formation characteristics of n-heptane/butanol isomers blends in laminar diffusion flames.** Energy, 211:118714, 2020.

[15] CHENG, X.; LI, Y.; XU, Y.; LIU, Y. ; WANG, B.. **Study of effects of ammonia addition on soot formation characteristics in n-heptane co-flow laminar diffusion flames.** Combustion and Flame, p. 111683, 2021.

[16] SHEN, R.; JIAO, Z.; PARKER, T.; SUN, Y. ; WANG, Q.. **Recent application of computational fluid dynamics (CFD) in process safety and loss prevention: A review.** Journal of Loss Prevention in the Process Industries, 67:104252, 9 2020.

[17] PORTARAPILLO, M.; SARLI, V. D.; SANCHIRICO, R. ; BENEDETTO, A. D.. **CFD simulation of the dispersion of binary dust mixtures in the 20 l vessel.** Journal of Loss Prevention in the Process Industries, 67:104231, 9 2020.

[18] HANENE, Z.; ALLA, H.; ABDELOUAHAB, M. ; ROQUES-CARMES, T.. **A numerical model of an immiscible surfactant drop spreading over thin liquid layers using CFD/VOF approach.** Colloids and Surfaces A: Physicochemical and Engineering Aspects, 600:124953, 9 2020.

[19] DIAZ, P. V.; YOON, S.. **High-fidelity computational aerodynamics of multi-rotor unmanned aerial vehicles**. AIAA Aerospace Sciences Meeting, 2018(1266), 2018.

[20] KIECKHEFEN, P.; PIETSCH, S.; DOSTA, M. ; HEINRICH, S.. **Possibilities and limits of computational fluid dynamics–discrete element method simulations in process engineering: A review of recent advancements and future trends**. Annual Review of Chemical and Biomolecular Engineering, 11(1):397–422, 2020.

[21] KALOGIROU, S. A.. **Artificial intelligence for the modeling and control of combustion processes: a review**. Progress in Energy and Combustion Science, 29(6):515–566, 2003.

[22] WANG, Q.; HESTHAVEN, J. S. ; RAY, D.. **Non-intrusive reduced order modeling of unsteady flows using artificial neural networks with application to a combustion problem**. Journal of Computational Physics, 384:289–307, 2019.

[23] MCQUARRIE, S. A.; HUANG, C. ; WILLCOX, K. E.. **Data-driven reduced-order models via regularised operator inference for a single-injector combustion process**. Journal of the Royal Society of New Zealand, 51(2):194–211, 2021.

[24] BRUNTON, S. L.; KUTZ, J. N.. **Data-Driven Science and Engineering: Machine Learning, Dynamical Systems, and Control**. Cambridge University Press, 2019.

[25] BRUNTON, S. L.; NOACK, B. R. ; KOUMOUTSAKOS, P.. **Machine learning for fluid mechanics**. Annual Review of Fluid Mechanics, 52(1):477–508, 2020.

[26] LECUN, Y.; BENGIO, Y. ; HINTON, G.. **Deep learning**. Nature, 521:436–444, 2015.

[27] PYTA, L.; ABEL, D.. **Online model adaption of reduced order models for fluid flows**. IFAC-PapersOnLine, 50(1):11138–11143, 2017.

[28] XIAO, X.; FANG, F.; BUCHAN, A. G.; PAIN, C. C.; NAVON, I. M. ; MUGGERIDGE, A.. **Non-intrusive reduced order modelling of the Navier-Stokes equations**. Computer Methods in Applied Mechanics and Engineering, 293:522–541, 2015.

[29] ANGRA, S.; AHUJA, S.. **Machine learning and its applications: A review.** Proceedings of the 2017 International Conference On Big Data Analytics and Computational Intelligence, ICBDACI 2017, p. 57–60, 10 2017.

[30] SUN, H.; BURTON, H. V. ; HUANG, H.. **Machine learning applications for building structural design and performance assessment: State-of-the-art review.** Journal of Building Engineering, 33:101816, 1 2021.

[31] GOGAS, P.; PAPADIMITRIOU, T.. **Machine learning in economics and finance.** Computational Economics 2021 57:1, 57:1–4, 2 2021.

[32] LIBBRECHT, M. W.; NOBLE, W. S.. **Machine learning applications in genetics and genomics.** Nature Reviews Genetics, 16:321–332, May 2015.

[33] SHARMA, R.; KAMBLE, S. S.; GUNASEKARAN, A.; KUMAR, V. ; KUMAR, A.. **A systematic literature review on machine learning applications for sustainable agriculture supply chain performance.** Computers & Operations Research, 119:104926, 7 2020.

[34] BIKMUKHAMETOV, T.; JÄSCHKE, J.. **Combining machine learning and process engineering physics towards enhanced accuracy and explainability of data-driven models.** Computers & Chemical Engineering, 138:106834, 7 2020.

[35] RAI, R.; SAHU, C. K.. **Driven by data or derived through physics? a review of hybrid physics guided machine learning techniques with cyber-physical system (CPS) focus.** IEEE Access, 8:71050–71073, 2020.

[36] ZHAO, X.; SHIRVAN, K.; SALKO, R. K. ; GUO, F.. **On the prediction of critical heat flux using a physics-informed machine learning-aided framework.** Applied Thermal Engineering, 164:114540, 1 2020.

[37] DA COSTA RAMOS, L.; DI MEGLIO, F.; FIGUEIRA DA SILVA, L. F. ; MORGENTHALER, V.. **Reduced order model of laminar premixed inverted conical flames.** In: AIAA SCITECH FORUM, Orlando, USA, 2020.

[38] ANANTHKRISHNAN, N.; DEO, S. ; CULICK, F. E. C.. **Reduced-order modeling and dynamics of nonlinear acoustic waves in a combustion chamber.** Combustion Science and Technology, 177(2):221–248, 2005.

[39] CHAKRAVARTHY, S. R.; ROWAN, S. L.; CELIK, I. B.; GUTIERREZ, A. D. ; ESCOBAR VARGAS, J.. **A reduced order model for the design of oxy-coal combustion systems**. Journal of Combustion, 2015(943568):1–9, 2015.

[40] WANG, Q.; HESTHAVEN, J. S. ; RAY, D.. **Non-intrusive reduced order modeling of unsteady flows using artificial neural networks with application to a combustion problem**. Journal of Computational Physics, 384:289–307, 2019.

[41] AVERSANO, G.; FERRAROTTI, M. ; PARENTE, A.. **Digital twin of a combustion furnace operating in flameless conditions: reduced-order model development from CFD simulations**. Proceedings of the Combustion Institute, 38(4):5373–5381, 2021.

[42] ALOMAR, A.; NICOLE, A.; SIPP, D.; RIALLAND, V. ; VUILLOT, F.. **Reduced-order model of a reacting, turbulent supersonic jet based on proper orthogonal decomposition**. Theoretical and Computational Fluid Dynamics, 34:49—-77, 2020.

[43] SWISCHUK, R.; KRAMER, B.; HUANG, C. ; WILLCOX, K.. **Learning physics-based reduced-order models for a single-injector combustion process**. AIAA Journal, 58(6):2658–2672, 2020.

[44] TURNS, S. R.. **An Introduction to Combustion: Concepts and Applications**. McGraw-Hill, 2nd edition, 2006.

[45] POINSOT, T.; VEYNANTE, D.. **Theoretical and Numerical Combustion**. Edwards, 2nd edition, 2005.

[46] JIN, Y.; SHAW, B.. **Computational modeling of n-heptane droplet combustion in air–diluent environments under reduced-gravity**. International Journal of Heat and Mass Transfer, 53(25):5782–5791, 2010.

[47] MARAGKOS, G.; BEJI, T. ; MERCI, B.. **Advances in modelling in CFD simulations of turbulent gaseous pool fires**. Combustion and Flame, 181:22–38, 2017.

[48] ANSYS. **Ansys fluent 12.0 theory guide**. ANSYS. 10 Oct 2021 <https://www.afs.enea.it/project/neptunius/docs/fluent/html/th/node1.htm>, 2009.

[49] KAZAKOV, A.; FRENKLACH, M.. **Reduced reaction sets based on gri-mech 1.2**. The Combustion Laboratory at the University of California, Berkeley. 20 Nov. 2019 <http://combustion.berkeley.edu/drm/>, 1984.

[50] GAUTHIER, G. P.; WATSON, G. M. G. ; BERGTHORSON, J. M.. **An evaluation of numerical models for temperature-stabilized CH_4/air flames in a small channel**. Combustion Science and Technology, 184(6):850–868, 2012.

[51] LABAHN, J. W.; STANKOVIĆ, I.; DEVAUD, C. B. ; MERCI, B.. **Comparative study between conditional moment closure (CMC) and conditional source-term estimation (CSE) applied to piloted jet flames**. Combustion and Flame, 181:172–187, 2017.

[52] HOERLLE, C.; ZIMMER, L. ; PEREIRA, F.. **Numerical study of CO_2 effects on laminar non-premixed biogas flames employing a global kinetic mechanism and the flamelet-generated manifold technique**. Fuel, 203:671–685, 2017.

[53] KANG, X.; SUN, B.; WANG, J. ; WANG, Y.. **A numerical investigation on the thermo-chemical structures of methane-oxygen diffusion flame-streets in a microchannel**. Combustion and Flame, 206:266–281, 2019.

[54] DE CASTRO, R. R.; FIGUEIRA DA SILVA, L. F.. **Experimental study of soot volume fraction and temperatue of laminar non-premixed ethylene-air flames**. In: 25TH ABCM INTERNATIONAL CONGRESS OF MECHANICAL ENGINEERING, Minas Gerais, Brazil, 2019.

[55] YOUNG, T. R.; BORIS, J. P.. **A numerical technique for solving stiff ordinary differential equations associated with the chemical kinetics of reactive-flow problems**. The Journal of Physical Chemistry, 81:2424–2427, 1977.

[56] JI, W.; QIU, W.; SHI, Z.; PAN, S. ; DENG, S.. **Stiff-PINN: Physics-informed neural network for stiff chemical kinetics**. Journal of Physical Chemistry A, 125:8098–8106, 9 2021.

[57] GARCÍA, A. M.; RENDON, M. A. ; AMELL, A. A.. **Combustion model evaluation in a CFD simulation of a radiant-tube burner**. Fuel, 276(25):118013, 2020.

[58] HIREMATH, V.; REN, Z. ; POPE, S. B.. **Combined dimension reduction and tabulation strategy using ISAT–RCCE–GALI for the efficient implementation of combustion chemistry**. Combustion and Flame, 158(11):2113–2127, 2011.

[59] MARROCU, M.; AMBROSI, D.. **Mesh adaptation strategies for shallow water flow**. International Journal for Numerical Methods in Fluids, 31:497–512, 1999.

[60] KALLINDERIS, Y.; VIJAYAN, P.. **Adaptive refinement-coarsening scheme for three-dimensional unstructured meshes**. AIAA Journal, 31(8):1440–1447, 5 1993.

[61] ROBBINS, B. A.; GRIFFITHS, D. V.. **Soda: A serial fortran library for adaptation of structured meshes**. Lecture Notes in Civil Engineering, 125:927–934, 5 2021.

[62] OOI, E. T.; MAN, H.; NATARAJAN, S. ; SONG, C.. **Adaptation of quadtree meshes in the scaled boundary finite element method for crack propagation modelling**. Engineering Fracture Mechanics, 144:101–117, 8 2015.

[63] DANNENHOFFER, J.; BARON, J.. **Grid adaptation for the 2-D Euler equations**. AIAA Paper, 85(484), Jan. 1985.

[64] ANSYS. **Gradient adaption approach**. ANSYS. 10 Mar 2020 <https://www.afs.enea.it/project/neptunius/docs/fluent/html/th/node395.htm>, 2009.

[65] DA COSTA RAMOS, L.. **Numerical study of an unstable premixed laminar flame and numerical Luenberger observers**. Thesis, Université Paris sciences et lettres, Sept. 2021.

[66] TREFETHEN, L. N.; BAU, D.. **Numerical Linear Algebra**. Society for Industrial and Applied Mathematics, USA, 1st edition, 1997.

[67] VIANA, F. A. C.; HAFTKA, R. T. ; STEFFEN, V.. **Multiple surrogates: how cross-validation errors can help us to obtain the best predictor**. Structural and Multidisciplinary Optimization, 39:439–457, 2009.

[68] BEN SALEM, M.; ROUSTANT, O.; GAMBOA, F. ; TOMASO, L.. **Universal prediction distribution for surrogate models**. SIAM/ASA Journal on Uncertainty Quantification, 5:1086–1109, 2017.

[69] WANG, S.; JIAN, G.; XIAO, J.; WEN, J. ; ZHANG, Z.. **Optimization investigation on configuration parameters of spiral-wound heat exchanger using genetic aggregation response surface and multi-objective genetic algorithm**. Applied Thermal Engineering, 119:603–609, 2017.

[70] ANSYS. **Twin Builder 2021 R1 - Static ROM Components**. ANSYS. Twin Bulder Help, December 2020.

[71] OSTERTAGOVÁ, E.. **Modelling using polynomial regression**. Procedia Engineering, 48:500–506, 2012.

[72] AVERSANO, G.; D'ALESSIO, G.; COUSSEMENT, A.; CONTINO, F. ; PARENTE, A.. **Combination of polynomial chaos and kriging for reduced-order model of reacting flow applications**. Results in Engineering, 10:100223, 2021.

[73] SMOLA, A. J.; SCHÖLKOPF, B.. **A tutorial on support vector regression**. Statistics and Computing, 14:199–222, 2004.

[74] LANCASTER, P.; SALKAUSKAS, K.. **Surfaces generated by moving least squares methods**. Mathematics of Computation, 37(155):141–158, 1981.

[75] BEN SALEM, M.; TOMASO, L.. **Automatic selection for general surrogate models**. Structural and Multidisciplinary Optimization, 58:719–734, 2018.

[76] MLYNARCZYK, P.. **Numerical optimization methods comparison based on the CFD conduction-convection heat transfer case**. International Journal of Numerical Methods for Heat & Fluid Flow, 29:2080–2092, 2019.

[77] LUBOZ, V.; BAILET, M.; GRIVOT, C. B.; ROCHETTE, M.; DIOT, B.; BUCKI, M. ; PAYAN, Y.. **Personalized modeling for real-time pressure ulcer prevention in sitting posture**. Journal of Tissue Viability, 31:54–58, 2018.

[78] CANO, J.-R.; GUTIÉRREZ, P. A.; KRAWCZYK, B.; WOŹNIAK, M. ; GARCÍA, S.. **Monotonic classification: An overview on algorithms, performance measures and data sets**. Neurocomputing, 341:168–182, 2019.

[79] EKATERINARIS, J. A.. **High-order accurate, low numerical diffusion methods for aerodynamics**. Progress in Aerospace Sciences, 41(3-4):192–300, 2005.

[80] XIE, B.; DENG, X.; LIAO, S. ; XIAO, F.. **Arbitrary high-order non-oscillatory scheme on hybrid unstructured grids based on multi-moment finite volume method**. Journal of Computational Physics, 424:109841, 2021.

[81] OBERKAMPF, W. L.; TRUCANO, T. G.. **Verification and validation in computational fluid dynamics**. Progress in Aerospace Sciences, 38(3):209–272, 2002.

[82] JUNQUEIRA, N. L.; FIGUEIRA DA SILVA, L.; DA COSTA RAMOS, L. ; DE PAULA, I. B.. **The influence of the learning data on the reduced order model of laminar non-premixed flames**. In: PROCEEDINGS OF THE 26TH ABCM INTERNATIONAL CONGRESS OF MECHANICAL ENGINEERING - COBEM 2021, online, 2021.